Building and Environment 165 (2019) 106373

Contents lists available at ScienceDirect

Building and Environment

journal homepage: www.elsevier.com/locate/buildenv

# The optimal tuning, within carbon limits, of thermal mass in naturally ventilated buildings

Salmaan Craig

*School of Architecture, Faculty of Engineering, McGill University, Montréal, QC, Canada*

ARTICLE INFO

*Keywords:*
Thermal mass
Natural ventilation
Thermal resilience
Materials design
Life cycle analysis
Thermal optimization
Low carbon

ABSTRACT

The topic of study is how to choose primary materials for minimal environmental impact while integrating as many functions into them as possible. Values for mathematical ratios are found, showing how to optimize the proportions of a building made with internal thermal mass. The mass is coupled with buoyancy ventilation in a natural thermal feedback cycle, driven by the daily swing of ambient temperature. This way, the primary material controls the structure, temperature, and ventilation. The ratios give the balance of dimensions needed to keep the thermal exchanges optimally synchronized. On one side of the balance, there is the ventilation openings and the height of the building. On the other side of the balance, there is the surface area, thickness, and thermal properties of the mass. Examples show how to take these ratios and materialize them into possible design options. That is, how they can shape the development of an architectural concept from part to whole, including the spatial organization of the building. The results suggest that thin-shell structures of minimum weight, and even timber buildings, can be optimally tuned.

## 1. Introduction

What proportions should a thermally massive building have? How should the thermal mass be distributed? Should the “massing” change with the choice of material? Recent studies on termite air-conditioning, revealing a feedback loop between thermal mass and buoyancy ventilation, suggest we still have much to learn [1–4].

Builders have intuitively harnessed the heat storage capacity of stone, brick, and earth for millennia [5–7]. Since the middle of the 20th century, engineers have used mathematical analysis and computer models to simulate the dynamics of thermal mass [6,8–11]. In the last three decades, building scientists have made increasingly accurate descriptions of temperature-driven ventilation, such as what happens when buoyant airflow and thermal mass are bound together by the ambient temperature swing in a natural feedback loop [12,13]. How to synchronize these ambient heat exchanges is the focus of this paper. The analysis shows how to make optimal adjustments to the form, height, mass, and openings of a building, based on ratios that balance the accumulation of heat inside the mass with its later release by thermal venting.

### 1.1. Radical integration

Thermal mass is widely recognized as an opportunity for greater material integration between structural and thermal design [14]. In the next decade, building design teams may be forced to shrink and simplify the material inventories of their design proposals to meet strict limits on greenhouse gas emissions [15–17]. As well as using construction materials in smaller quantities and for longer lifetimes, the emphasis will be on finding intelligent ways of organizing, shaping, and upgrading these materials, so that ancillary building products and artificial climate control are less needed, and renovation, reuse, and recycling are more straightforward in later life-stages [18,19].

Energy efficiency at the operational stage (occupancy phase) of buildings continues to receive significant attention from researchers. However, building design reforms have so far failed to face a creeping trend: the increasing complexity of material assemblies, arbitrarily sourced from a globalized supply chain. Using add-ons to increase energy efficiency may have serious consequences, causing rebound effects [20,21] or shifting the environmental burdens from the occupancy stage to other life cycle stages [22]. Carbon, like money, has a time value [23]. The chances of avoiding runaway climate change are diminishing. A kilogram of emissions avoided today is worth more than a kilogram of emissions hypothetically saved in the future.

In a systematic review of 102 studies, Pomponi and Moncaster identified 17 strategies for mitigating and reducing embodied carbon in the built environment [24]. In their analysis, no single mitigation strategy stood out as potent in isolation. Instead, several approaches

*E-mail address:* salmaan.craig@mcgill.ca.

https://doi.org/10.1016/j.buildenv.2019.106373
Received 15 July 2019; Received in revised form 22 August 2019; Accepted 23 August 2019
Available online 28 August 2019
0360-1323/ © 2019 The Author. Published by Elsevier Ltd. This is an open access article under the CC BY license (http://creativecommons.org/licenses/BY/4.0/).

need combining. Better design, the use of materials with lower embodied carbon, the re-use of embodied-carbon-intensive materials, and stronger policy drivers all emerged as crucial elements for a quicker transition to a low carbon built environment.

One challenge for designers, therefore, is how to choose primary materials for minimal environmental impact while integrating as many functions into them as possible. Then there is less need for emissions-intensive materials and mechanical equipment in the first place. For this to happen, the properties of primary materials must be fully exploited and enhanced, by geometrical design from part to whole. Harnessing natural thermal feedbacks is also essential. Then the surrounding environment can play a role in thermoregulation, replacing artificial components.

It may be some time before the industry establishes a consensus on how to accurately account for the carbon-dioxide emissions associated with construction. Efforts are underway to improve the quality of emissions data, make them widely and freely available, and to standardize the accounting and reporting procedures [25–27]. However, as one study recently highlighted [28], the discrepancy between results from different carbon accounting methods can be significant—larger, even, than the savings either method estimates for alternative design schemes. This scale of uncertainty is disabling for decision-makers. It seems to propagate in proportion to the number of components: the more complex the material assembly, the more difficult it is to get an accurate picture of the potential web of ecological upheaval. Radical material integration could, therefore, result in a double dividend: real reductions in carbon-dioxide emissions, and more reliable predictions of these reductions.

### 1.2. Strategic comparisons

In the construction industry, the materials supply chain is decentralized, and technical knowledge is distributed among independent, competing organizations [29]. At any moment in this complex and unpredictable web of social relations (Fig. 1), technical expertise is liable to fragment, forcing the piecemeal resolution of technical concerns. Opportunities for integration across functional systems slip by the wayside (Fig. 2), increasing the complexity of the materials inventory. Engineering models must do their work against the background of this shared context. The results of a model can help to establish consensus and steer the activities of other project contributors and stakeholders. In the early stages of design, architects develop a range of volumetric forms to facilitate discussion with project contributors and stakeholders. These so-called “massing studies” do not need to be geometrically detailed; their purpose is to help build consensus on which issues and ideas to prioritize and develop further.

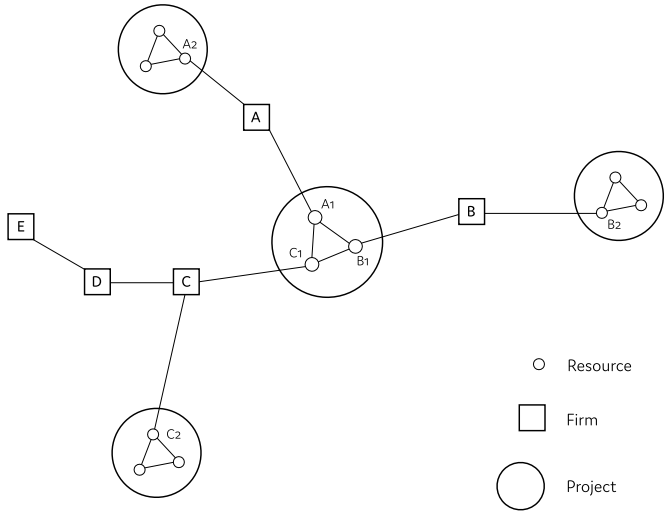


**Fig. 1.** A construction project in its dynamic, social context (adapted from [29]). Firms A, B, and C have different expertise. They must balance their resources competitively and simultaneously across several projects. Technical knowledge is therefore distributed among loosely coupled communities. It can be organized according to any project but is liable to fragment if social relations weaken or breakdown.

The ratios [31] presented in this paper can be used as a *strategic model* for thermal and material massing. The model is meant to help design teams [32,33] produce and compare options in the preliminary stages, improving their ability to integrate technical systems and understand the associated environmental impacts. The ratios are not suitable as a *forecasting model*, i.e. to estimate future patterns of energy use and thermal comfort in absolute terms. Forecasting models require detailed input information: their prediction quality improves as design decisions settle and finalize. In contrast, a strategic model must establish what constitutes a well-performing design and show what the requisite balance of technical parameters are—but without predetermining the final design configuration. Strategic models are most effective when they are stripped down to their essential relations so that the causal workings are transparent to all members of the project team and everyone can agree that the model is a suitable proxy for reality.

Experienced analysts may use a strategic model to frame the parameters of debate. For instance, they may treat the model as an opportunity to inform project stakeholders on recent research in adaptive comfort [34–48], advocating for natural ventilation principles to be incorporated into the schematic design. In such a case, the analyst may try to show the cumulative influence of passive design measures on the floating or free-running temperature; that is, how the interior temperature evolves without active thermostatic control. With the frequency and intensity of heatwaves increasing all over the world [49–51], the free-running temperature provides a basis for sizing cooling plants [52–54] but also indicates whether interior conditions will stay safely within physiological limits for heat-stress, particularly when there is a blackout or when occupants cannot afford to run or install mechanical cooling. Comparing the free-running temperature to thresholds for adaptive comfort and dangerous heat-stress can, therefore, indicate the thermal resilience of a proposed design [55-58].

Here is an example of one possible calculation flow using the method presented in subsequent sections. The design team decides on the free-running temperature (relative to the exterior swing of temperature), the rate of buoyancy ventilation (to satisfy the needs of occupants and their activities), the thermal massing material (which may serve a structural function, too), and the notional height of the building (which co-determines the potential energy for driving the buoyancy ventilation). The equations then give the optimum thickness and surface area of that material (operating as externally insulated thermal mass) and the necessary size of ventilation openings (i.e. the effective open area). The team can then evaluate a range of options that achieve the same performance but with different geometries and massing materials (and repeat the process with different inputs as necessary).

## 2. Previous work

Thermal mass refers to the ancient practice of configuring spaces and materials so that the materials passively store heat during the day then release it at night; as a result, the interior stays naturally cool in the hottest parts of the day [59–63]. Where to place thermal mass in the building envelope—The innermost layer? The outermost layer? Both?—is a recent concern. Modern life is increasingly spent indoors with technological accouterments that generate extra heat, while building envelopes are now composed of several material layers, each with specific functions to accommodate the need for insulation and airtightness. The most direct way to absorb excess heat generated by interior activities is to expose the mass on the innermost layer (i.e. so it is an “internal mass”). External insulation and shading then protect the mass from ambient heat and baking sunshine. However, the absorbed

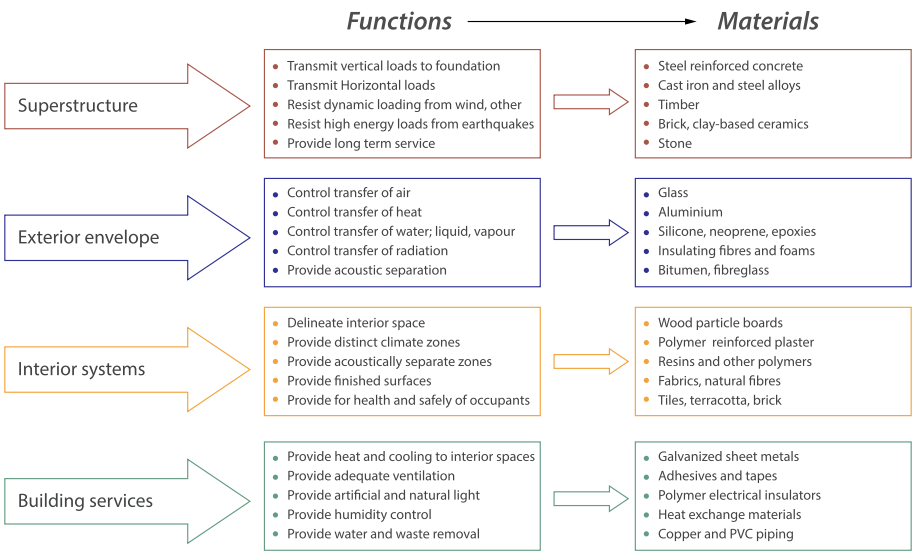


**Fig. 2.** The functional systems of a modern building (adapted from [30]). Dividing up functions in this way helps to organize the expertise and activities of project contributors. But it can also mask opportunities for functional integration, and wastefully increase the size and scope of the materials inventory.

interior heat must somehow be discharged at night for the cooling effect to work the following day. This discharging can be done by ventilation.

Buoyancy ventilation, otherwise known as stack ventilation, refers to the practice of configuring spaces and openings so that the airflow is driven spontaneously by the temperature difference between inside and outside. In updraft mode, warm air rises and escapes out the top while cooler air floods in from below to replace the evacuating air. In downdraft mode, the cycle reverses: cooler air spills out from below and warmer air floods in from above. In recent years, there have been major advances in the engineering theory of buoyancy ventilation, otherwise known as the art of "emptying a filling box" [64–67]. Researchers have solved problems such as how to keep the emptying air from stratifying to save energy on colder days [68,69], how to differentially size openings in a multistorey building according to the vertical pressure gradient [70,71], and how the cooling from thermal mass or another source changes the flow to a downdraft [72–75].

Unlike stochastic wind forces, buoyancy forces can be balanced and harnessed in a stable and continuous feedback loop. Sustaining this loop in temperate weather is straightforward. Demand for ventilation exists when people are present: these people and their activities generate heat; this heat can power the ventilation; therefore, balance the temperature and flow rate by sizing the stack and adjusting the openings accordingly. The balancing act is not quite so simple in hot weather. Some cooling is needed to cancel the heat loads and to keep the interior below ambient temperature. Most or all of this cooling can come from thermal mass—so long as the ventilation and heat storage cycles are well synchronized.

### 2.1. Coupling mass and buoyancy

In 2003, Yam, Li, and Zheng [76] were the first to examine the nonlinear coupling between an internal thermal mass and buoyancy ventilation. Yam et al. derived differential equations to describe this nonlinear behavior and solved them numerically. The results showed a close-to-periodic variation of the interior temperature. This finding led them to conclude that harmonic analysis could reasonably represent the coupling, assuming an average heat transfer coefficient for the surface.

Inspired by this finding, Holford and Woods [12] undertook a thorough mathematical investigation of the coupling in 2007. They parameterized the relationships between diffusion through an internal mass, convection at its surface, and buoyancy ventilation, and described the relationships in terms of dimensionless ratios. They then solved the differential equations numerically for a range of scenarios, assuming periodic (i.e. harmonic) variations in the ambient temperature. Using the same parameters, they then built an approximate lumped model, and systematically compared the results of this approximate model to the more detailed numerical version—and found good agreement. Significantly, their lumped model is discretized into four interacting temperature signals—the exterior temperature, the interior temperature, the surface temperature of the internal mass, and the lumped temperature of the mass (Fig. 3). The ability to accurately estimate the coupled surface and interior temperature—using analytical shortcuts—represented a significant advance in the thermal mass literature.

In 2008, unaware of the work of Holford and Woods, Zhou et al. [77] added to the work of Yam et al. (Li was a common co-author) by outlining a method to solve for the interior surface temperature, based on harmonic analysis. Their approach also considered periodic losses and gains from exterior insulation (both Yam et al. and Holford and Woods had assumed adiabatic boundary conditions, i.e. perfect insulation). In 2011, interested in the effects of massive floors, ceilings, and furniture, Zhou et al. [78] showed how to bundle the buffering effects of different pieces of thermal mass into a 'virtual sphere', posing the question: why relegate thermal mass to the envelope at all?

In 2009, Lishman and Woods [13] characterized thresholds for how natural ventilation behaves in thermally massive buildings. These thresholds depend on the unsteady balance between buoyancy forces, wind forces, interior heating, and heat storage. They found that the balance of these forces plays out on short and long time-scales, making for a surprising range of possible evolutionary paths and final flow regimes. For instance, if the interior heat load suddenly changes, the regime may rapidly switch from wind-driven to buoyancy-driven flow, only to switch back hours later once the thermal mass adjusts to the changes. Understanding these path-dependencies is important, so that they can be strategically avoided or harnessed by design.

In 2012, unaware of the work of Lishman and Woods (but citing other important works, e.g. [79–81]), Faure and Roux [82] analyzed the short and long term effects that thermal mass has on natural displacement ventilation, focusing on features such as the stratification height and how this interface buoys or "overshoots" before settling to steady-state. In 2016, Yang and Guo [83] analyzed the coupling between internal mass and buoyancy ventilation using Fourier components at multiple frequencies, to understand the temperature evolution of the system when driven by more realistic ambient conditions—that

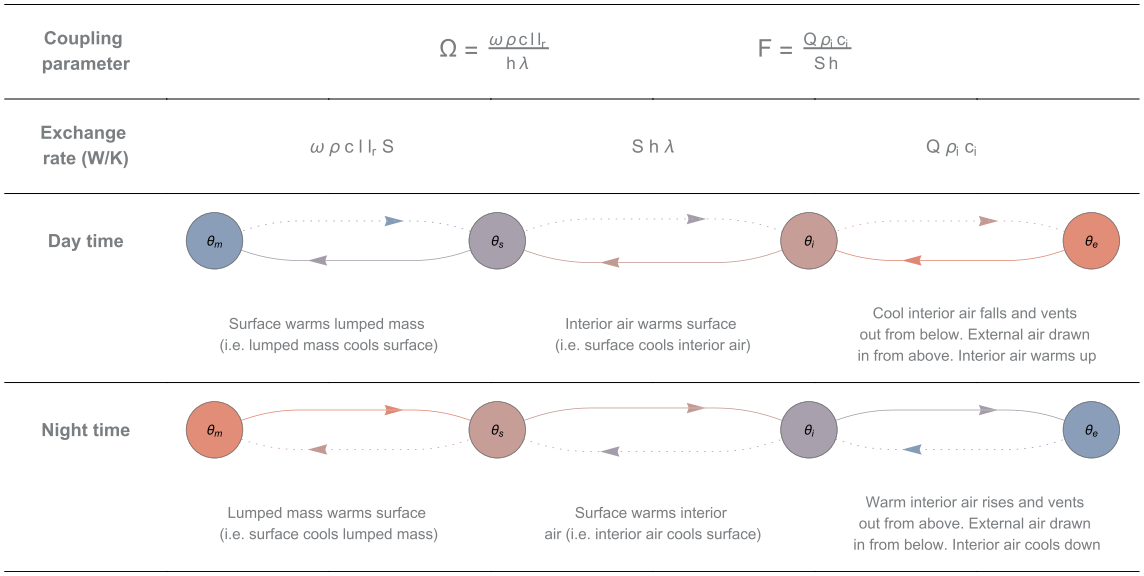


**Fig. 3.** The natural feedback loop between internal thermal mass and buoyancy ventilation, as parameterized by Holford & Woods [12].

is, an exterior temperature signal which is not quite sinusoidal. Comparing their predictions to data from a small physical experiment, they confirmed that these more realistic excitations produced ventilation flow rates that are *anharmonic* (but which are nevertheless predictable with Fourier analysis).

In 2018, Bastien and Athienitis [84,85] gave a skilled demonstration of how to design thermal mass inside greenhouses and solaria. They did some parametric design studies using the frequency response method (combining Laplace transforms and Fourier analysis), then followed this up with detailed annual simulations using the finite-difference method. The parametric studies allowed them to compare different approaches to optimizing the thermal mass thickness. They argued that the best approach for solaria was to control the delay between when the mass absorbs most sunshine and when it releases this heat.

Lots of research has been published in the thermal mass literature since the turn of the century, especially for efficient methods to simulate thermal mass in arbitrary configurations [9,10,86–94]. However, it seems that very little of this new knowledge has been distilled into ratios that help architects and planners to proportion thermal mass buildings properly—particularly in light of the material integration and cooling challenges posed by climate change. Of all the studies on thermal mass, the work by Holford and Woods seems to be the most promising as a basis for the necessary design guidance.

### 2.2. The Holford and Woods model

Fig. 3 describes the feedback loop between thermal mass and buoyancy ventilation, as modelled and parameterized by Holford and Woods [12]. The parameters $F$ and $\Omega$ are dimensionless numbers (i.e. they are ratios without units). They control the relative heat exchange between ventilation and thermal mass, respectively. When $F \sim \Omega \sim 1$, the heat exchange between the ventilation and the thermal mass is balanced. When $\Omega > > F$, the thermal mass dominates—the interior temperature is highly damped, and the air changes are relatively low. When $F > > \Omega$, the ventilation dominates—the air changes are relatively high, and the thermal mass hardly affects the interior temperature.

The two ends of the casual chain in Fig. 3 are unconnected, and this highlights one of the most significant simplifications in the Holford and Woods model. The model assumes an internal mass, meaning there is no heat transfer at the outer face. The mass is *indirectly* connected to the external environment, via the interior air. These adiabatic boundary conditions are equivalent to perfect exterior insulation, or adjacent spaces with perfectly replicated thermal conditions.

Fig. 4 shows the influence of F and Ω on the interior, surface, and mass temperatures during a 24-hour cycle. The temperature signals are normalized, so they are relative to maximum 1 and minimum −1 while the time is expressed in radians. The outside temperature varies periodically:

$$T_e(t) = T_0 + \Delta T \cos(\omega t) \tag{2.1}$$

Where $T_0$ is the mean daily temperature, $T_0 = (T_{min} - T_{max})/2$, ΔT is the temperature increment above the mean, $\Delta T = |T_{max} - T_0|$, and $\omega$ is the angular frequency, $\omega = 2\pi/86400$. The dimensionless time and temperature are, respectively:

$$\tau = \omega t \tag{2.2}$$

$$\theta = \frac{(T - T_0)}{\Delta T} \tag{2.3}$$

The four temperatures in the system are defined as follows. The exterior temperature:

$$\theta_e = \cos(\tau) \tag{2.4}$$

The interior temperature (assuming perfectly mixed air):

$$\theta_i = \frac{\cos(\tau - \Phi_i)}{A_i} \tag{2.5}$$

The surface of the thermal mass facing the interior:

$$\theta_s = \frac{\cos(\tau - \Phi_s)}{A_s} \tag{2.6}$$

And the temperature of the thermal mass:

$$\theta_m = \frac{\cos(\tau - \Phi_m)}{A_m} \tag{2.7}$$

The thermal mass is modelled as a lumped mass, meaning that, unlike a real mass, there are no temperature gradients inside it. A lumped mass has a single evolving temperature that represents the equivalent work of a real mass. The lumped mass temperature signal is close to, but not the same as, the average temperature of a real mass. Significantly, Holford and Woods were also able to find a shortcut for solving the surface temperature (see below). In this way, it was possible to get an accurate representation of the coupling between the mass-surface-interior without having to solve for the temperature gradients inside the mass.

To plot the temperature signals, one needs to know the attenuation

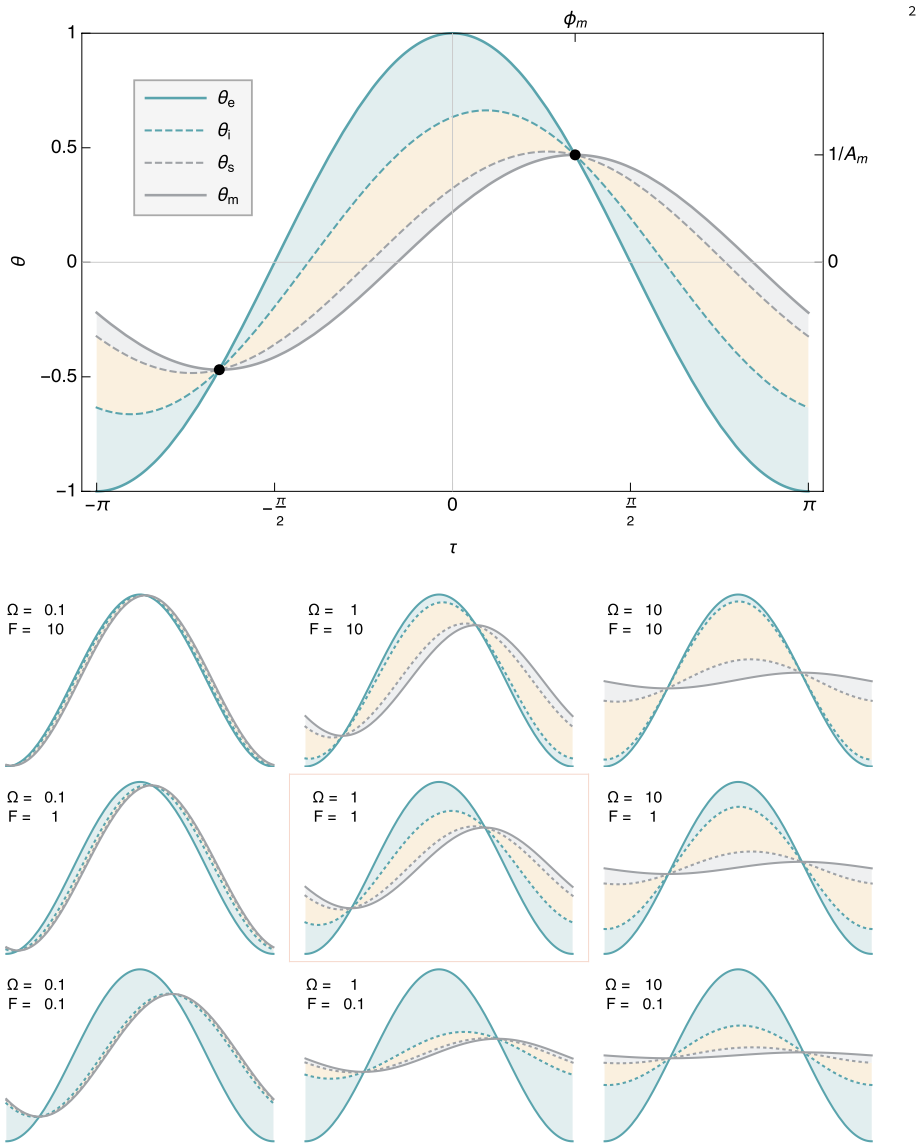


**Fig. 4.** The influence of the ventilation parameter F and the massing parameter Ω on the relative floating temperatures, $\theta_i$, $\theta_s$, $\theta_m$ (i.e. interior, surface, mass), driven by cyclic changes in the external temperature $\theta_e$over a period of $2\pi = 24$ h, after Holford & Woods [12]. The surface temperature delay of the thermal mass is arbitrarily fixed at $\lambda = 0.75$ in all graphs.

($A$) and the phase lag ($\Phi$). The reciprocal of the attenuation ($1/A$) is the peak temperature, relative to $\theta_e = 1$. The phase lag is the time delay of the peak temperature, relative to $\tau = 0$. The attenuation for the interior temperature is:

$$A_i = \frac{A_m}{\sqrt{1+\Omega^2}} \tag{2.8}$$

The attenuation for the surface temperature is:

$$A_s = \frac{A_m}{\sqrt{1+\Omega^2(1-\lambda)^2}} \tag{2.9}$$

And the attenuation for the mass temperature is:

$$A_m = \frac{1}{\cos(\Phi_m)} \tag{2.10}$$

The parameters λ and Ω will be defined shortly. The phase lag of the interior temperature is:

$$\Phi_i = \Phi_m - \tan^{-1}(\Omega) \tag{2.11}$$

The phase lag of the surface temperature is:

$$\Phi_s = \Phi_m - \tan^{-1}((1-\lambda)\Omega) \tag{2.12}$$

Algebraic substitution reveals that the temperature definitions all include $\Phi_m$:

$$\theta_i = \sqrt{1+\Omega^2}\,\cos(\Phi_m)\cos(\tau - \Phi_m + \tan^{-1}(\Omega)) \tag{2.13}$$

$$\theta_s = \sqrt{1+(1-\lambda)^2\,\Omega^2}\,\cos(\Phi_m)\cos(\tau - \Phi_m + \tan^{-1}((1-\lambda)\Omega)) \tag{2.14}$$

$$\theta_m = \cos(\Phi_m)\cos(\tau - \Phi_m) \tag{2.15}$$

How to solve for the mass phase lag, $\Phi_m$? The first option is to numerically solve the differential equations that define their lumped parameter model:

$$\Omega\frac{d\theta}{d\tau} = \theta_i - \theta_m$$
$$0 = \lambda(\theta_m - \theta_i) + F(\theta_e - \theta_i)|\theta_e - \theta_i|^{1/2} \tag{2.16}$$

Alternatively, Holford and Woods found two shortcuts for estimating $\Phi_m$:

$$\left(\frac{\tan(\Phi_m)}{\Omega} - 1\right)^6 = \left(\frac{\lambda^2}{\Omega F^2}\right)^2 \left(1 + \frac{1}{\Omega^2}\right)(1 + \tan^2(\Phi_m)) \tag{2.17}$$

$$\frac{\tan(\Phi_m)}{\Omega} = 1 + 1.07\left(\frac{\lambda^2}{\Omega F^2}\right)^{1/3} \tag{2.18}$$

They compared the accuracy of Equation (2.16), Equation (2.17), and Equation (2.18) against a full numerical model (which represented diffusion through the mass with finite-differences and which allowed the ventilation to vary non-linearly). They found that Equation (2.16) and Equation (2.17) stay accurate to within 0.1% and 1%, respectively, across parameter space—even for very extreme scenarios (e.g. when a very thick mass combines with a very high rate of ventilation, leading the surface temperature to stray far from the mass temperature). Equation (2.18) is less consistent; it is only reasonably accurate for balanced scenarios.

Since $\Phi_m$ is determined by parameters Ω, λ, and $F$, these three parameters alone control the entire system. The massing parameter Ω is defined as:

$$\Omega = \frac{\xi(\cosh(2\eta) - \cos(2\eta)) + \eta(\sinh(\eta) - \sin(2\eta))}{\eta(\sinh(2\eta) + \sin(2\eta))} \tag{2.19}$$

Where $\xi$ is the potential rate of heat storage compared to the rate of surface heat transfer:

$$\xi = \frac{\omega \rho c l}{h} \tag{2.20}$$

And $l$ is the thickness of the mass, $\rho c$ is the volumetric heat capacity of the mass material, and $h$ is the surface heat transfer coefficient. The parameter $\eta$ is the ratio of the layer thickness to the depth of thermal penetration:

$$\eta = l\sqrt{\frac{\omega}{2\alpha}} \tag{2.21}$$

Where $\alpha$ is the thermal diffusivity of the mass material. The massing parameter can also be written as:

$$\Omega = \frac{\xi\, l_r}{\lambda} = \frac{\omega\, \rho c\, l\, l_r}{h\, \lambda} \tag{2.22}$$

Where $l_r$ is the fraction of material thickness needed for the lumped mass to do the equivalent work of the real mass:

$$l_r = \frac{(\cosh(2\eta) - \cos(2\eta))}{\eta(\sinh(2\eta) + \sin(2\eta))} \tag{2.23}$$

And λ is a factor which, by approximating the temperature gradients inside the mass, determines the surface temperature:

$$\lambda = \frac{1}{1 + \frac{\eta(\sinh(2\eta) - \sin(2\eta))}{\xi(\cosh(2\eta) - \cos(2\eta))}} \tag{2.24}$$

This surface temperature factor ranges between $0 < \lambda < 1$. When $\lambda = 1$, there are no temperature gradients inside the mass, so $\theta_s = \theta_m$. When $\lambda \to 0$ , the surface temperature strays further and further away from the mass temperature; as a result, the mass stores heat less and less efficiently.

Finally, we can define the ventilation heat exchange parameter, which compares the ventilation heat exchange to the surface heat exchange at the surface:

$$F = \frac{Q\, \rho_i c_i}{S\, h} \tag{2.25}$$

Where $\rho_i c_i$ is the volumetric heat capacity of air, $S$ is the surface area of mass exposed to the interior air, and the rate of ventilation, $Q$, is:

$$Q = A^* \sqrt{\beta\, g\, H\, |T_e - T_i|} \tag{2.26}$$

Where $A^*$ is the effective area of ventilation openings (see [95]), $\beta$ is the thermal expansion coefficient of air, and $H$ is the stack height. The rate of ventilation, powered by buoyancy, depends on the interior temperature—which in turn depends on the rate of ventilation (c.f Fig. 3). Holford and Woods suggest setting $|T_e - T_i| = \triangle T$ in Equation (2.26) to obtain a reference ventilation rate. Alternatively, we define an average ventilation rate, based on the normalized mean temperature difference:

$$Q = A^* \sqrt{\beta\, g\, H\, \triangle T\, |\theta_e - \theta_i|_{mean}} \tag{2.27}$$

According to the integral mean value theorem, the mean temperature difference is:

$$\left|\theta_e - \theta_i\right|_{mean} = \frac{1}{b-a}\int_a^b |\theta_e - \theta_i| d\tau \tag{2.28}$$

Where $b = \Phi_m - \pi$ and $a = \Phi_m$ mark the beginning and end of half a cycle. Substituting equations Equation (2.4) and Equation (2.13) and completing the integration gives:

$$|\theta_e - \theta_i|_{mean} = \frac{-2\,\Omega\cos(\Phi_m) + 2\sin(\Phi_m)}{\pi} \tag{2.29}$$

## 3. Analysis

§2 identified the work of Holford and Woods [12] as a promising basis for design guidance on how to proportion thermally-massive buildings. Using their parameterization, this section finds a new way to optimally synchronize the coupling of internal thermal mass and buoyancy ventilation.

### 3.1. The optimal tuning

The Holford and Woods model (c.f. §2.2) describes the coupling between internal thermal mass and buoyancy ventilation. This coupling is controlled by two non-dimensional parameters: $F/\lambda$ (the ratio of ventilation heat transfer to surface heat transfer) and Ω (the ratio of thermal storage to surface heat transfer). This section defines two optimal tunings for $F/\lambda$ and Ω. The two optimal tunings are associated with different damping coefficients, defined graphically in Fig. 5.

The first damping coefficient is the maximum difference between the interior and exterior temperature in a given cycle, $|\theta_e - \theta_i|_{peak}$. Let us call it the *peak venting temperature difference*, since it is the moment of maximum buoyancy ventilation. It occurs twice in a 24-hour cycle, but when exactly? As indicated in Figs. 4 and 5, all temperatures in the system converge at time $\tau = \Phi_m$. When this happens, the buoyancy ventilation momentarily ceases before switching direction from a daytime downdraft to a nocturnal updraft. If the minimum venting temperature difference occurs at time $\tau = \Phi_m$, it follows that the peak venting temperature difference occurs midway through a half-cycle at time $\tau = \Phi_m - \pi/2$. Subtracting equation (2.12) from 2.4 and substituting the definition for $\tau$ gives:

$$|\theta_e - \theta_i|_{peak} = -\Omega\cos(\Phi_m) + \sin(\Phi_m) \tag{3.1}$$

Now is necessary to substitute a definition for $\Phi_m$. As discussed in §2.3, Equation (2.18) is less accurate than Equation (2.17), but it does have the advantage of not needing to be solved iteratively. Moreover, recall from §1 that strategic comparisons, not absolute forecasts, are the focus of this paper. Substituting Equation (2.18) gives:

$$\left|\theta_e - \theta_i\right|_{peak} = \frac{1.07\left(\frac{\lambda^2}{F^2\,\Omega}\right)^{1/3}\Omega}{\sqrt{1 + \left(\Omega + 1.07\left(\frac{\lambda^2}{F^2\,\Omega}\right)^{1/3}\Omega\right)^2}} \tag{3.2}$$

Fig. 6 shows a contour plot of the peak venting temperature difference as a function of $F/\lambda$ and Ω. Notice how, for every increment of $|\theta_e - \theta_i|_{peak}$, there is an optimal pairing of Ω and $F/\lambda$. This ideal tuning is defined by the curve:

$$(F/\lambda)_{max} = \sec(1.07\Omega^{4/3}) - 1 \tag{3.3}$$

Optimal design values can be found by solving Equation (3.2) and

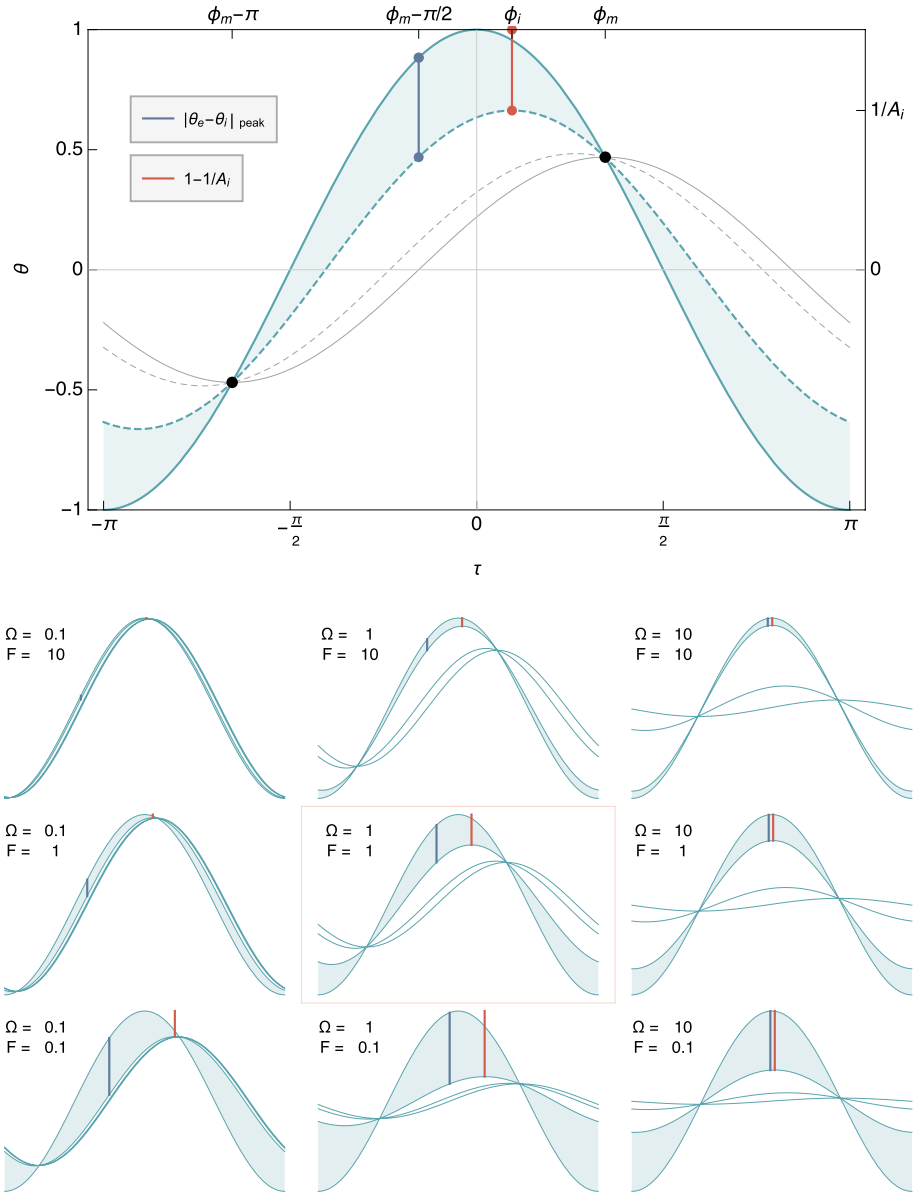


**Fig. 5.** The definition of two damping coefficients: the peak venting temperature difference, which is shown in blue and occurs at time $\tau = \Phi_m - \pi/2$, and the attenuating temperature difference, $1 - 1/A_i$, which is shown in red and occurs at time $\tau = \Phi_i$. The graphs show the influence of F and Ω on both kinds of damping coefficient. The surface temperature delay of the thermal mass is arbitrarily fixed at $\lambda = 0.75$ in all graphs. (For interpretation of the references to colour in this figure legend, the reader is referred to the Web version of this article.)

Equation (3.3) simultaneously. To do this, one needs to consider $F/\lambda$ as a single variable in Equation (3.2) (i.e. so that $\left(\frac{\lambda^2}{F^2\,\Omega}\right) = \left(\frac{1}{a^2\,\Omega}\right)$, where $a = F/\lambda$). The independent values for F and λ can be found later. For instance, solving Equation (3.2) and Equation (3.3) tells us that to optimize for $|\theta_e - \theta_i|_{peak} = 0.5$, one should design the thermal mass such that $\Omega = 0.94$; this will maximize the $F/\lambda$ parameter such that $F/\lambda = 0.83$. Now recall that λ predicts the surface temperature delay due to temperature gradients inside the mass, and depends on the choice of the material. If calculations for one material show that $\lambda = 0.9$, then $F = 0.83 * 0.9 = 0.747$ (see §4.1 for a more detailed example).

In this way, one can evaluate the effect of the thermal properties of materials fairly. All material masses can be sized to achieve the same optimal value for the massing parameter Ω—it is just a matter of finding the correct thickness. However, because of differences in thermal properties, different material masses can't have the same values for both Ω *and* λ. The differences in λ manifest as differences in surface temperature, and the surface temperature regulates the power of buoyancy ventilation. Therefore, everything else being equal, materials with a lower λ are less efficient as thermal mass because *they produce less ventilation*.

Fig. 5 defines a second damping coefficient, which occurs at time $\tau = \Phi_i$. Let us call it the *attenuating temperature difference:*

$$1 - \frac{1}{A_i} = 1 - \sqrt{1 + \Omega^2}\,\cos(\Phi_m) \tag{3.4}$$

Substituting equation (2.11) gives:

$$1 - \frac{1}{A_i} = 1 - \frac{\sqrt{1+\Omega^2}}{\sqrt{1+\left(\Omega + 1.07\left(\frac{\lambda^2}{F^2\,\Omega}\right)^{1/3}\Omega\right)^2}} \tag{3.5}$$

Fig. 7 shows a contour plot of the attenuating temperature difference as a function of $F/\lambda$ and Ω. Once more, notice how, for every temperature increment, there is an optimal value of Ω for which $F/\lambda$ is maximized. This ideal tuning is defined by the curve:

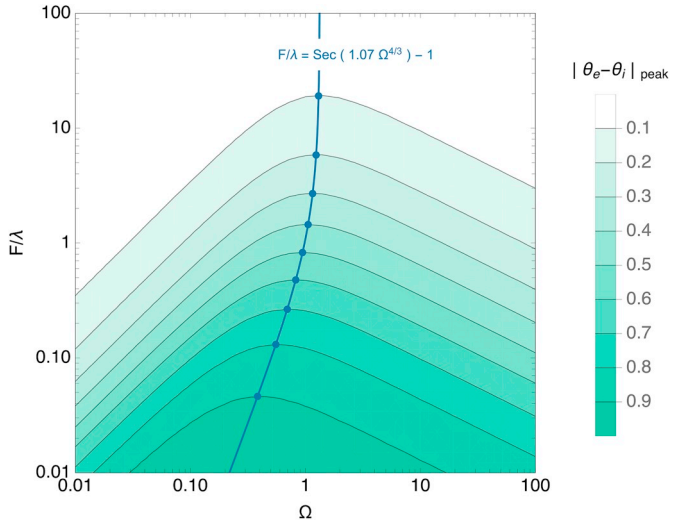


**Fig. 6.** Contour plots of the peak venting temperature difference $|\theta_e - \theta_i|_{peak}$. The blue curve locates the optimal pairings of Ω and F/λ. (For interpretation of the references to colour in this figure legend, the reader is referred to the Web version of this article.)

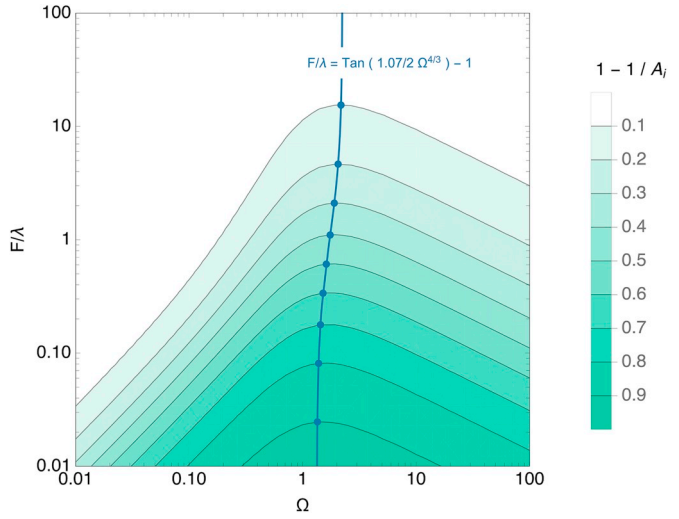


**Fig. 7.** Contour plots of the attenuating temperature difference $1 - 1/A_i$. The blue curve locates the optimal pairings of Ω and F/λ. (For interpretation of the references to colour in this figure legend, the reader is referred to the Web version of this article.)

$$(F/\lambda)_{max} = \tan\left(\frac{1.07}{2}\Omega^{4/3}\right) - 1 \tag{3.6}$$

Like before, optimal design values can be found by solving Equation (3.5) and Equation (3.6) simultaneously. For instance, to achieve $1 - 1/A_i = 0.5$ , one should design the thermal mass such that $\Omega = 1.62$; this will maximize the ventilation parameter such that $F/\lambda = 0.61$.

Notice that the optimal values for both damping coefficients are quite similar. The attenuating temperature difference is associated with slightly larger values for optimal Ω and slightly smaller values for maximum F/λ. These small differences in the ideal tuning can have a large impact on the physical dimensions of the architecture, as the massing studies of §4 will show.

### 3.2. Surface heat transfer

The previous subsection described how to optimize thermal mass and natural ventilation in a feedback cycle, by finding ideal pairs F/λ and Ω to synchronize the coupled heat exchanges. §4 explores the implications of these ideal proportions for sizing buildings and choosing materials. However, before doing this, a fair estimate of the surface heat transfer coefficient, $h$, is essential, as both $F/\lambda$ and Ω depend on it.

At the surface of an internal mass, sensible heat exchange occurs by convection and radiation. The rate of convection determines the strength of coupling between the thermal mass and buoyancy ventilation. Any radiation heat transfer has an indirect, but consequential, influence on this coupling.

Surface convection inside rooms can be driven naturally by surface temperatures, forcibly by nearby air flows, or by a mixture of natural and forced convection. Forced convection on an interior surface may be a consequence of breeze from fans, vents, and open windows, plumes from warm people and equipment, or a larger circulation pattern powered by buoyancy inside the space. In this paper, natural convection is the focus. Unlike forced convection, natural convection is guaranteed to happen in the thermal feedback cycle described in this paper, and will do so in synchronization with the temperature evolution of the system. If there is a particular scenario in which forced convection may be significant, its influence on the baseline natural convection can be estimated by consulting the correlations in the literature [96–98], or by running high-resolution transient simulations with computational fluid dynamics incorporating the thermal energy equation [99].

The heat transfer coefficient for natural convection varies according to the interaction between thermal and gravitational forces (Fig. 8). The heat transfer coefficient is smallest when the orientation of the surface ($\gamma \rightarrow 180^\circ$) impedes warm air from rising or cool air from falling. In other orientations, the heat transfer coefficient is larger. Turbulence ensues when viscous forces no longer dominate, and the boundary layer de-laminates from the surface.

Fig. 8 was computed using an algorithm recommended by Raith by and Hollands (see [100,101]). The algorithm evaluates five empirical correlations for the heat transfer coefficient: a pair of correlations for surfaces at inclination $\gamma = 0^\circ$ (one for laminar flow, one for turbulent flow); a pair for surfaces at inclination $\gamma = 90^\circ$ (laminar and turbulent); and one for surfaces at inclination $\gamma = 180^\circ$ (gravity keeps the flow practically quiescent in this case). For intermediate angles (e.g. $\gamma = 77^\circ$), some other equations combine results from two reference angles (e.g. $\gamma = 0^\circ$ and $\gamma = 90^\circ$) after balancing their weights asymptotically. The five empirical correlations are not shown here. However, with some minor exceptions, they all take the general form:

$$Nu = \frac{h_c\, k}{L} = m\, Ra^n \tag{3.7}$$

Where $Nu$ is the Nusselt number, $h_c$ is the average heat transfer coefficient for natural convection, $k$ is the thermal conductivity of the fluid (in this case, air), $L$ is the characteristic length of the surface (e.g. the ratio of the area to the perimeter), $n$ is a fraction less than 1 (usually 1/4 or 1/3), $m$ is an empirically derived constant, and $Ra$ is the Rayleigh number:

$$Ra = \frac{g\,\beta\,L^3\,(T_s - T_i)}{\nu\,\alpha} \tag{3.8}$$

Where $\nu$ and $\alpha$ are the viscosity and the thermal diffusivity of the air, respectively. While conducting the calculations, the influence of the characteristic length (L) was evidently weak for panel sizes bigger than approximately 1 by 1 m. Mathematically speaking, the weakening influence of $L$ is because the exponent $n$ in Equation (3.7) asymptotically levels out the influence of the Rayleigh number (even though $Ra \propto L^3$). Physically speaking, air is not very viscous: on a large surface, the natural convection boundary layer soon reaches full turbulence, even if powered by a small temperature difference. Therefore, Fig. 8 (which assumes a surface of 3 by 3 m) can be used to approximate the natural heat transfer coefficient for many surface sizes inside rooms, at any inclination, from concrete table tops to triple-height walls.

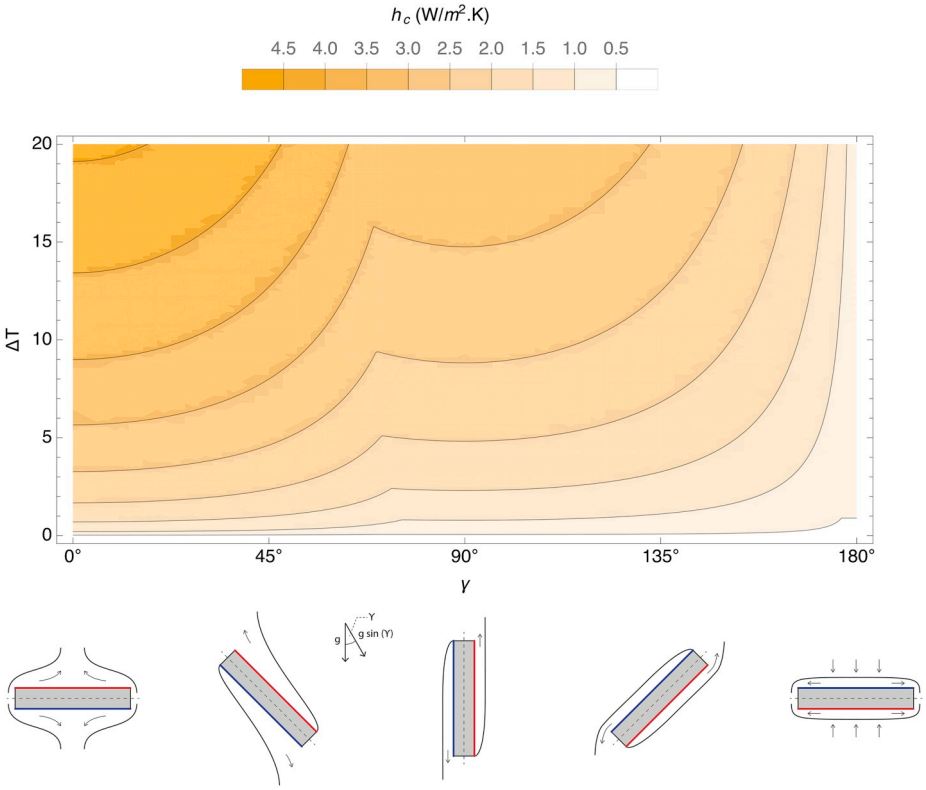


**Fig. 8.** Contours of the average heat transfer coefficient, h, due to natural convection from a hot or cold surface. It varies according to the temperature difference, the rotation angle, and the size of the surface (here 3 × 3 m).

For an estimate of the *average* convection heat transfer coefficient, it is necessary to know the mean temperature difference between the surface and the interior. According to the integral mean value theorem:

$$\left|\theta_i - \theta_s\right|_{mean} = \frac{1}{b-a}\int_a^b |\theta_i - \theta_s| \mathrm{d}\tau \tag{3.9}$$

Where $b = \Phi_m - \pi$ and $a = \Phi_m$ mark the beginning and end of half a cycle. Substituting equations Equations (2.13) and (2.14) and completing the integration gives:

$$|\theta_i - \theta_s|_{mean} = \frac{2\,\lambda\,\Omega\cos(\Phi_m)}{\pi} \tag{3.10}$$

The average surface heat flux can now be defined as:

$$q_{mean} = h\,\Delta T\,|\theta_s - \theta_i|_{mean} \tag{3.11}$$

Where $h$ is the total heat transfer coefficient:

$$h = h_c + h_r \tag{3.12}$$

And $h_r$ is the radiation heat transfer coefficient:

$$h_r \simeq \sigma\,\varepsilon\,4\,T_0^3 \tag{3.13}$$

Where $\sigma$ is the Stefan-Boltzmann constant and $\varepsilon$ is the average emissivity of the surfaces. Equations (3.11) and (3.12) assume that surface radiation, like surface convection, is governed by the temperature difference between the surface and the interior. Let us interrogate the validity of this assumption by imagining an idealized scenario. Consider a fictional body inside the space that follows the interior temperature and exchanges radiant energy uniformly with all surrounding surfaces. This fictional radiator does not heat the air directly, but it does heat the air indirectly at a later time (because it heats or cools the mass, and later the mass heats or cools the air). Consider also that when there is no radiator present, and the idealized space is empty, there is no net radiation exchange between the enclosing surfaces since they are all the same temperature.

### 3.3. Interior heat loads

Can this fictional radiator be used as a proxy for internal heat loads? In a real room, there are many kinds of heat sources and sinks, of different sizes, locations, and time signatures. Locally, they heat or cool the interior air by convection. Remotely, they heat or cool other surfaces by radiation. Real interior heat loads are not evenly distributed in space, nor are they harmoniously synchronized in time. Moreover, recall that the direction of heating for the fictional radiator is $\theta_i > \theta_s$ during the day, switching to $\theta_i < \theta_s$ during the night. Real interior heat loads may diminish or disappear at night, but they do not spontaneously turn into sources of cooling.

Despite these inconsistencies and contradictions, a fictional radiator (which follows the interior temperature) is still a relevant proxy for average heat loads. This radiator cannot represent realistic heating distributions in time or space, because a harmonic model cannot account for the possible knock-on effects of asymmetrical or asynchronous loads on the temperature evolution of the system. Nevertheless, evaluating the effects of an average heat load is a useful starting point (c.f. §1.2 *strategic models*).

To apply this proxy for internal heat loads, the analyst must first evaluate the heat flux from the fictional radiator and decide if it needs increasing to meet any deficit in the expected average heat load. Meeting the deficit can be done by multiplying $h_r$ by some factor. Then the charging and discharging cycles must be balanced over the day. For instance, by assuming that the ventilation openings ($A^*$) are automatically increased at night, so the extra buoyancy ventilation matches the night cooling by the fictional radiant body.

Fig. 9 compares the cumulative surface heat transfer due to natural convection and radiation. The yellow portions of the graph show natural convection, which is present even when the interior space is empty. The red parts show emissions from a fictional radiator as a proxy for internal loads. The graphs are arranged in a grid with two columns, one for each damping coefficient: the left-hand column aligns with the peak

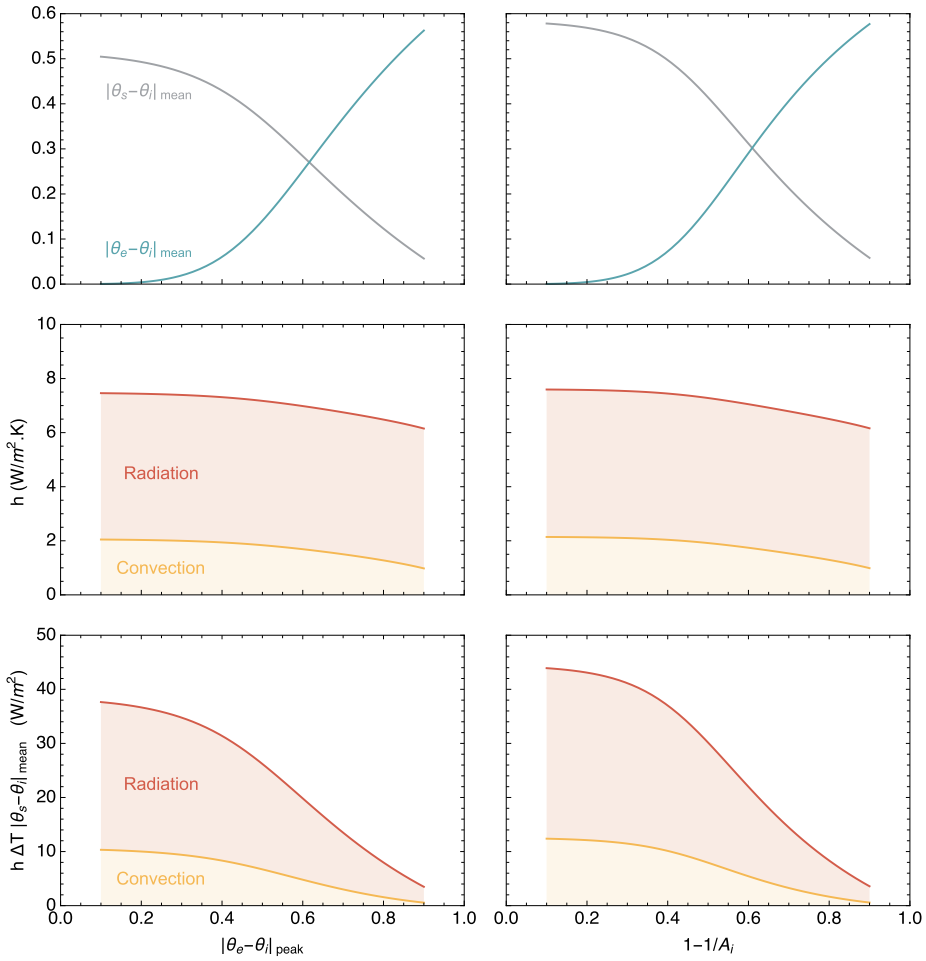


**Fig. 9.** Variation of surface heat transfer with $|\theta_e - \theta_i|_{peak}$ and.$1 - 1/A_i$

venting temperature difference $|\theta_e - \theta_i|_{peak}$; the right-hand column aligns with attenuating temperature difference $1 - 1/A_i$. The top row of graphs shows a governing trend: the larger the damping coefficient, the smaller the temperature difference between the surface and the interior air. This downturn leads to slight reductions in the heat transfer coefficient (W/m$^2$-K, see middle row), but considerable reductions in the surface heat flux (W/m$^2$, see bottom row).

Note that, in Fig. 9, the radiant heat transfer coefficient is defined by equation Equation (3.13), and the radiant heat flux is controlled by $|\theta_s - \theta_i|_{mean}$ in Equation (3.11) (i.e. the radiant heat flux has *not* been adjusted to equally represent internal loads for all values of either damping coefficient; in this way, the relative changes and possible deficits are clear to see). Furthermore, note that the heat flux is reported in terms of the unit surface area of the mass, not in terms of the unit floor area (which is how internal loads are typically presented).

To compute the results shown in Fig. 9, the environmental temperature was fixed at $\Delta T = 10$ and $T_0 = 20^{\circ}C$ (293.15 K). Optimal pairs of $F/\lambda$ and $\Omega$ are needed to calculate $|\theta_s - \theta_i|_{mean}$ for increments of $|\theta_e - \theta_i|_{peak}$ and $1 - 1/A_i$. This was done by simultaneously solving Equations (3.2) and (3.3) or Equations (3.5) and (3.6), assuming no surface temperature delay (i.e. $\lambda = 1$). The surface heat transfer was then computed following the procedure described in §3.2, assuming a large, 10 by 10 m vertical surface for the convection calculations.

## 4. Results and discussion

The previous section found optimal pairings for $F/\lambda$ and $\Omega$, and explained how to approximately account for internal loads by adjusting the heat transfer coefficient. This theory is now applied in some massing studies, which show the effect that optimal designs have on material quantities and physical proportions.

### 4.1. Materials comparison

Among practitioners, it is common knowledge that some materials are more effective as thermal mass because of their thermal properties. (Namely: the thermal conductivity, $k$ (W/m-K); the volumetric heat capacity, $\rho c$ (J/m$^3$-K); and the combination of these in a ratio called the thermal diffusivity, $\alpha = k/\rho c$ (m$^2$/s), which compares the internal rate of heat transfer to heat storage, indicating how quickly heat spreads through a material.) However, when it comes to examining thermal mass materials in action, it is difficult to draw conclusions that meaningfully influence design—particularly in the critical early stages—since it is hard to isolate the role that architectural properties play in the co-evolution of system temperatures. What proportions should a thermally massive building have? How should the thermal mass be distributed? Should the massing change with the choice of material? Without comprehensive answers to these questions, analysts, when studying the effects of thermal mass with dynamic models, have had little choice but to fix the dimensions of their control buildings arbitrarily [103–105] —until now.

Table 1 gives ranges of thermal properties for some standard construction materials [102]. Fig. 10 compares the efficiency of these materials as thermal mass when they are optimally tuned as part of a thermal feedback cycle (c.f. Fig. 3). That is, a building with internal mass that maximizes buoyancy ventilation for a given damping coefficient ($|\theta_e - \theta_i|_{peak}$, light shading; $1 - 1/A_i$, dark shading). Fig. 10 shows the layer thicknesses ($l$, bottom row) and the divergence in surface

**Table 1**
Candidates for thermal mass: representative ranges for thermal properties and $CO_2$ footprints [102].

| | k (W/m-K) | ρ c (J/m$^3$-K) | $CO_2$footprint (kg/m$^3$) |
|---|---|---|---|
| Steel | 51.5 ± 2.5 | (3.79 ± 0.20) × $10^6$ | 14135. ± 875. |
| Sandstone | 5.70 ± 0.30 | (2.16 ± 0.28) × $10^6$ | 87. ± 19. |
| Concrete | 1.6 ± 0.8 | (2.3 ± 0.4) × $10^6$ | 260. ± 53. |
| Glass | 1.00 ± 0.30 | (2.22 ± 0.15) × $10^6$ | 1850. ± 142. |
| Brick | 0.59 ± 0.14 | (1.49 ± 0.29) × $10^6$ | 402. ± 82. |
| Hardwood* | 0.46 ± 0.05 | (1.59 ± 0.18) × $10^6$ | − 400 ± 1300 |

*Values for *k* assume conduction is parallel to the grain. Values for $CO_2$ footprint range from net storage to net release. Notice how, per unit volume, timber can sequester carbon or be worse than concrete, depending on how the forest is managed.

temperatures (λ, top row) for different materials. The width of the coloured bands reflects the uncertainty associated with the thermal properties (c.f. Table 1); the dotted lines assume average values for these properties.

Fig. 10 is based on the same set of assumptions as Fig. 9(recall from §3.3 that the radiant heat flux varies with $|\theta_s - \theta_i|_{mean}$; it was *not* adjusted to model internal loads equally across all values of the damping coefficient). Fig. 10 can be reproduced with different inputs by following these three steps:

- Choose a damping coefficient to optimize for ($|\theta_e - \theta_i|_{peak}$ or $1 - 1/A_i$) and find the associated optimal values for Ω (c.f. §3.1)
- Estimate *h* by: (a) Consulting Figs. 8 and 9. Or (b) estimate $|\theta_s - \theta_i|_{mean}$by setting λ = 1. Use this result to compute *h* (c.f. §3.2), incorporating an estimate for internal heat loads as necessary (c.f. §3.3).
- Find the optimal thicknesses (l) and resulting surface temperature delays (λ) by simultaneously solving Equations (2.22), (2.23) and (2.24). (A first approximation can be made by assuming λ = 1, so that $l_r$ = 1 and Equation (2.22) reduces to Ω = ξ)

Fig. 10 reveals some general trends, which reflect the balance of thermal relationships.

- As either damping coefficient ($|\theta_e - \theta_i|_{peak}$ or $1 - 1/A_i$) increases, the optimal thickness reduces. This is because the massing parameter, Ω, and the surface heat flux, $h \triangle T\ |\theta_s - \theta_i|_{mean}$, reduce, too.
- Optimizing for the damping coefficient $|\theta_e - \theta_i|_{peak}$ results in relatively thinner masses, because this damping coefficient is associated with smaller values of Ω, and so requires less thermal capacity.
- The uncertainty associated with thermal properties can lead to significant discrepancies in optimal thickness—in the order of centimeters. In later stages of design, it is therefore important to obtain more accurate values for thermal properties, ideally with direct measurements of actual samples.

Moreover, Fig. 10 suggests several new findings regarding the efficiency of different construction materials as thermal mass:

- Some natural stones and concretes are particularly efficient as an internal thermal mass when optimally-tuned (which should come as no surprise since these materials have relatively high *k* and high ρc). However, *the ideal tuning adds new meaning to what constitutes an efficient thermal mass.* The plots show that, when optimized, sandstone and concrete have non-divergent surface temperatures (λ→1). Recall that F = (F/λ) *λ. Therefore, compared to other optimized masses, *these masses are able to produce more ventilation for a given damping coefficient*
- However, some concretes (those with lower *k* and ρc) do not perform as well. The function for λ (Equation (2.24)) is particularly sensitive in the range $1 \lesssim \eta \lesssim 2$ (c.f. Fig. 8.b. in Holford and Woods [12]). Optimally-tuned concrete is uniquely situated in this range, making it susceptible to sudden (and unexpected) drops in efficiency. Consider that the thermal properties of concrete (or any structural material for that matter) are rarely specified or measured in real projects.
- The graphs reveal many situations in which $l \lesssim 5$ cm, suggesting that thin-shell structures of minimum weight [106–112] may also be optimized for thermal mass and natural ventilation.
- Assuming the heat-flux is oriented parallel to the grain, optimally-tuned hardwood compares well against brick and not too poorly against concrete. (The thermal conductivity of hardwood perpendicular to the grain, and for softwoods in either grain orientation, are lower.) This suggests it is possible to use some timbers as internal thermal mass—with reasonable effect. These thermally resilient timber buildings could legitimately sequester carbon dioxide, so long as the timbers are sourced from sustainable, managed forests, and the buildings last longer than the growing cycles of these forests [113–117].
- While not analyzed here, the thermal properties of earthen materials [118] and high-density bamboo composites [119] suggest that these materials are promising candidates, too.

### 4.2. Fixed volume of material

The remainder of this section examines the consequences of the ideal tuning in terms of building dimensions, material quantities, and ventilation rates.

Fig. 11 shows how to distribute *a fixed amount* of concrete thermal mass inside an insulated cuboid of height H = 10 m. The floor area is variable, but constrained to the shape of a square ($W^2$), thereby defining the geometry of the ceiling and four walls where the mass is distributed. Since $V = S\ l$, optimally distributing a fixed volume of material (V) means finding the balance of surface area (S) and thickness (l) that:

- Meets a given damping coefficient (i.e. a design value for $|\theta_e - \theta_i|_{peak}$ or $1 - 1/A_i$ ), while;
- Maximizing the rate of buoyancy ventilation (Q).

The calculation flow for producing Fig. 11 follows these steps:

- Find the ideal tuning for Ω and $F/\lambda$ (c.f. §3.1)
- Estimate *h* and find *l* andλ (c.f. §4.1)
- Now $S = V/l$ and $Q = \frac{F\ S\ h}{\rho_i\ c_i}$ (c.f. Equation (2.25))
- Furthermore, though not shown in Fig. 11, $A* = \frac{Q}{\sqrt{\beta\ g\ H\ \Delta T\ |\theta_e - \theta_i|_{mean}}}$ (c.f. Equation (2.27))

Here are some things to bear in mind when reading Fig. 11:

- The concrete mix assumes mean values for thermal properties shown in Table 1. The environmental temperature and the rates of surface heat transfer are the same as those described in §3.3 and shown in Fig. 9.
- For the purposes of demonstration, the volume of concrete is arbitrarily fixed at V = {8, 27, 64} $m^3$.
- For reference, when the ratio of width to height is W/H = {1, 2, 3, 4}, the surface area of the thermal mass is S = {500, 1200, 2100, 3200} $m^2$
- For reference, a sufficient amount of ventilation for one person is typically 10 L per second. That is, Q = 0.01 $m^3$/s. Therefore, when the ventilation rate is Q = {0.1, 1, 10} $m^3$/s, there is enough fresh air for approximately {10, 100, 1000} people.

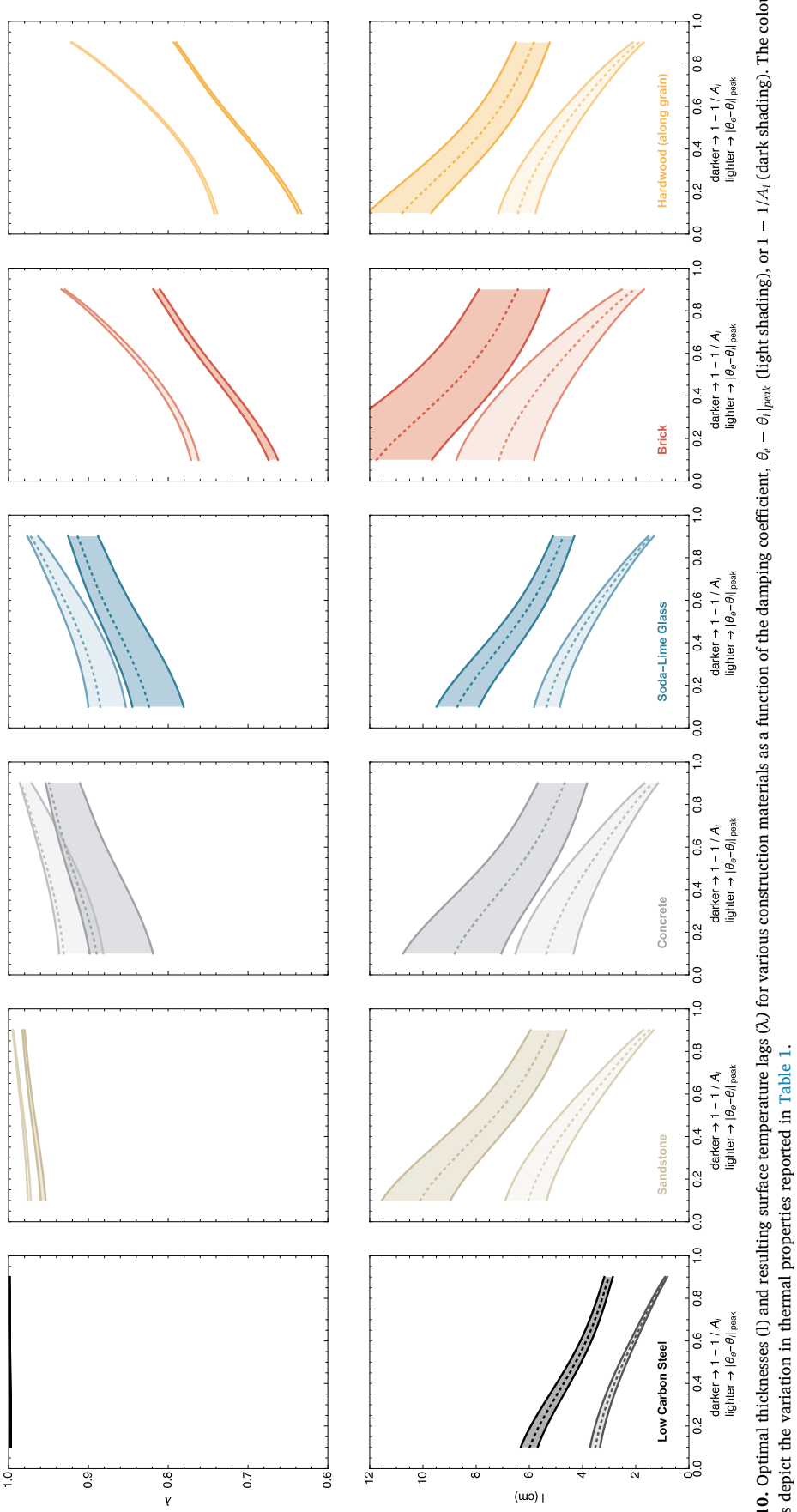


**Fig. 10.** Optimal thicknesses (l) and resulting surface temperature lags ($\lambda$) for various construction materials as a function of the damping coefficient, $|\theta_e - \theta_i|_{peak}$ (light shading), or $1 - 1/A_i$ (dark shading). The coloured bands depict the variation in thermal properties reported in Table 1.

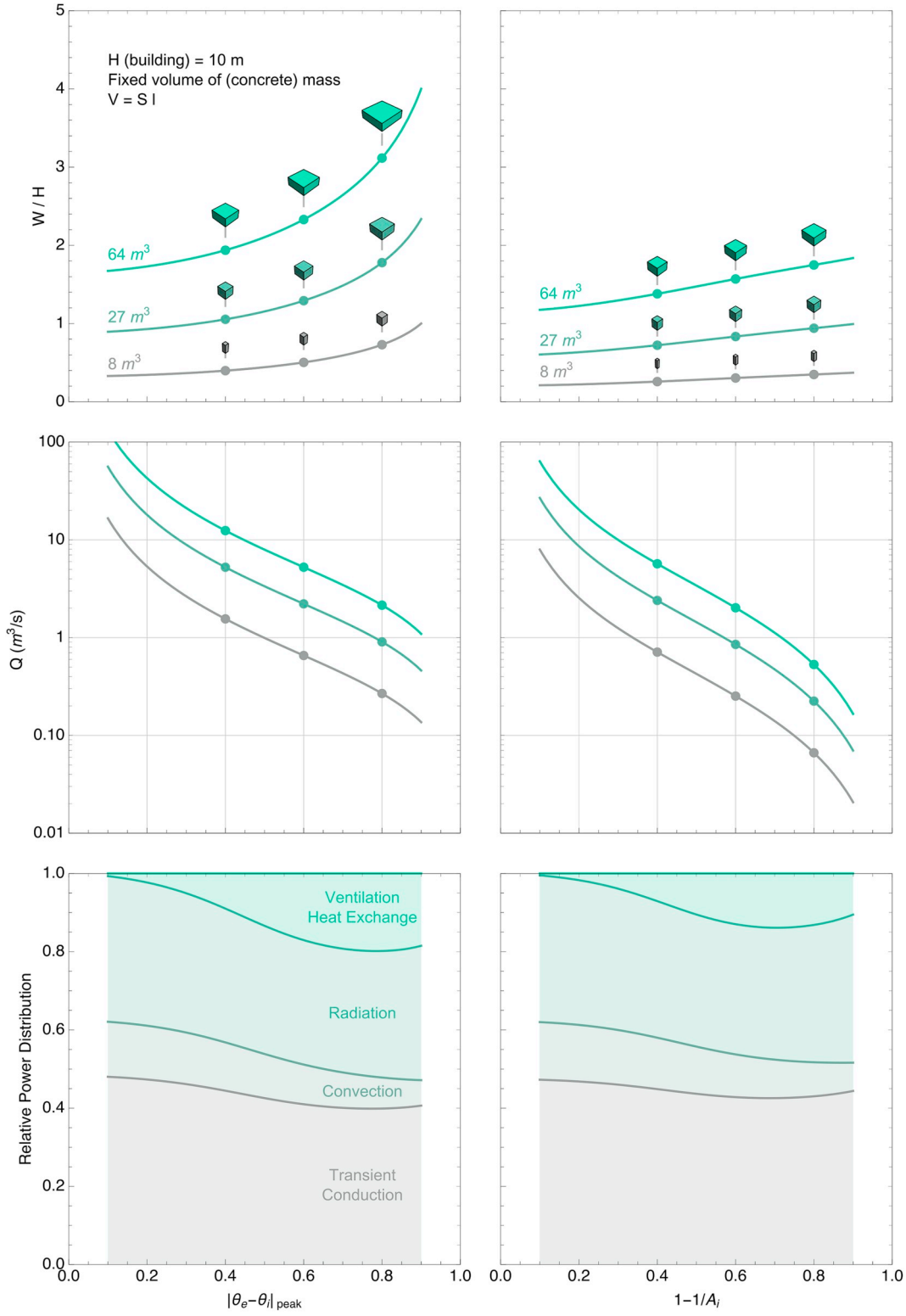


**Fig. 11.** The optimal distribution of a fixed amount of concrete thermal mass (V = S l) that maximizes buoyancy ventilation (Q) for a given damping coefficient ($|\vartheta_e - \vartheta_i|_{peak}$ or $1 - 1/A_i$).

Some general observations can be made:

- Optimizing for the attenuating temperature difference requires thicker masses, resulting in smaller buildings (compared to the peak venting temperature difference, when the material volume is fixed).
- The relative power distribution, shown in the bottom row of graphs, does not change with the volume constraint (since the balance of thermal exchanges is the same for each optimal case).

While it is unconventional to fix the amount of material before design commences, this strategy may be useful in the coming decade as carbon caps become better defined and more stringent.

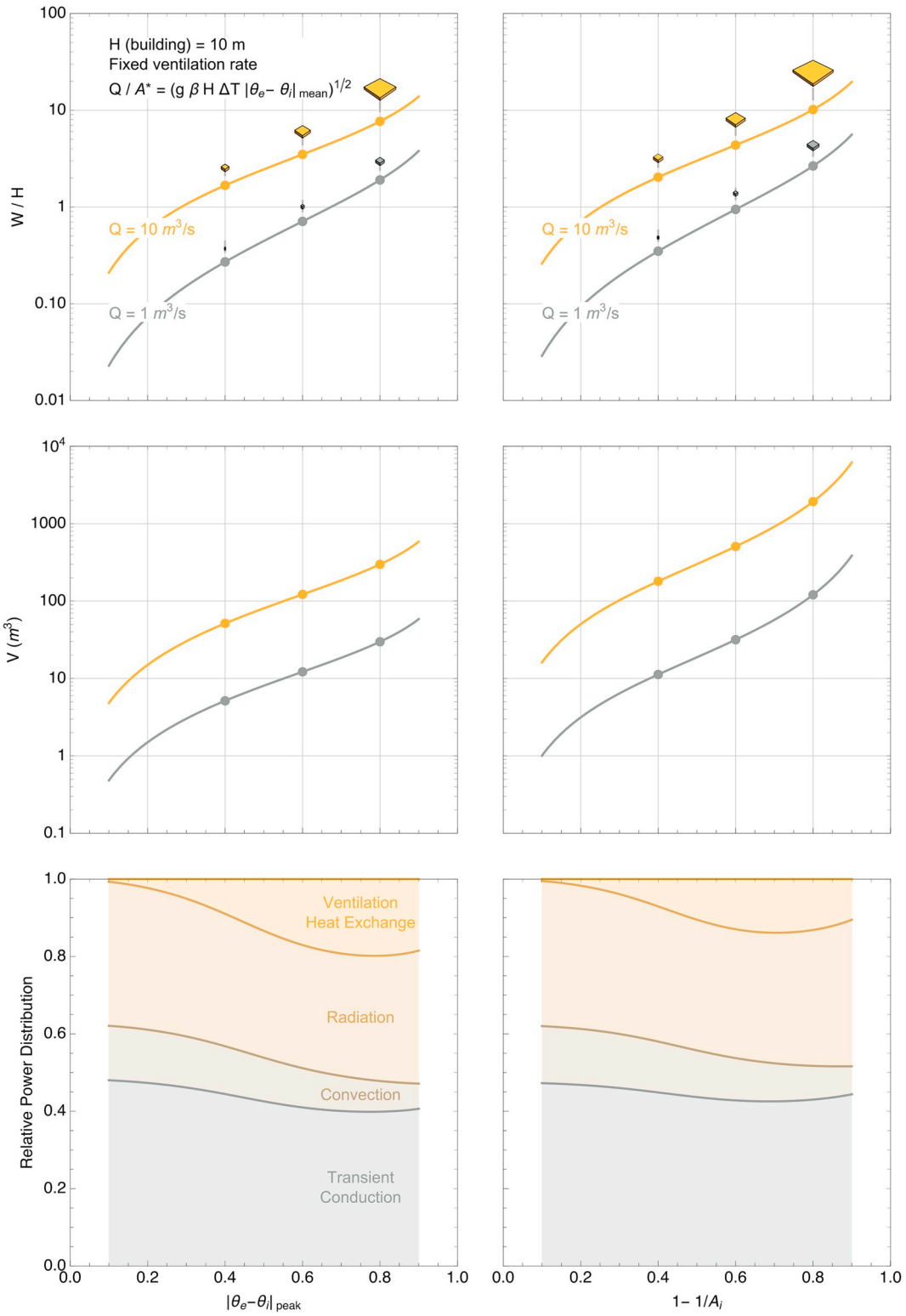


**Fig. 12.** Optimal quantities (V = Sl) and distributions (W/H) of thermal mass for a fixed ventilation rate (Q) to meet a target interior floating temperature (e-i peak or 1-1/Ai).

### 4.3. Fixed rate of ventilation

Having shown how to use the ideal tuning to compare massings made from the same volume of material, this subsection compares ideally-tuned massings that produce the same ventilation.

Fig. 12 shows how to distribute *the ideal amount* of concrete thermal mass inside an insulated cuboid of height H = 10 m. The rate of buoyancy ventilation is fixed at Q = {1, 10} $m^3/s$ to provide enough fresh air for approximately {10, 100} people. Since $V = S\,l$, finding the ideal volume of concrete (V) means finding the combination of surface area (S) and thickness (l) that:

- Meets a given damping coefficient (i.e. a design value for $|\theta_e - \theta_i|_{peak}$ or $1 - 1/A_i$ ), while;

- Meeting the target rate of buoyancy ventilation (Q).

The calculation flow for producing Fig. 12 follows these steps:

- Find the ideal tuning for Ω and $F/\lambda$
- Find $l$ and $\lambda$
- Now $S = \frac{Q\,\rho_i\,c_i}{F\,h}$ and $V = S\,l$

Here are some things to bear in mind when reading Fig. 12:

- The assumptions (thermal properties, environmental temperature, surface heat transfer) are the same as in Fig. 11.
- Unlike Fig. 11, the vertical axis for W/H is logarithmic
- The images of the cuboids are scaled to the largest cuboid in the graph (hence they appear smaller than the cuboids in Fig. 11).

Compared to Fig. 11, the ideal proportions (W/H) in Fig. 12 vary considerably, since there is no constraint on the material volume. One range worth taking a closer look at is the range of damping coefficient $0.6 \lesssim 1 - 1/A_i \lesssim 0.8$ when $Q = 1\,m^3/s$. These massings perform well without needing a very large surface ($W/H < 10$) or a very large amount of concrete ($V < 100\,m^3$).

Fig. 13 interrogates this range in more detail, using different geometries and comparing the efficacy of concrete to timber (hardwood, parallel to the grain, c.f. Table 1) as internal thermal mass. The buildings start as a hemisphere or a cube ($H = 10\,m$). Their shapes then 'morph' according to mathematically defined rules, which allow the surface area of the building to increase without taking up much extra land. As the surface area increases, so does the damping coefficient—though the ventilation is always the same. Bluer colours, therefore, indicate cooler buildings.

Fig. 13 shows three columns of "morph sequences". These morphologies are defined as follows:

- **Blobs.** These surfaces are defined by the Legendre polynomial $P_n(x)$ [120], plotted in spherical coordinates, such that: the radius is $r = 1 + c\,P_n(\cos(\varphi))\cos(\vartheta)$; the zenith (latitude) angles are $0 \le \varphi \le \pi$; and the azimuth (longitude) angles are $0 \le \vartheta \le \pi$. The coefficient $c$ (here set to $c = 1/4$) determines the "smoothness" of the polynomial and hence the smoothness of the blob. The integer $n$ increases the number of operations in the polynomial and hence the number of "wings" the blob has.
- **Castles.** The remaining two columns are populated by surfaces defined by fractals: a Sierpiński space-filling curve [121], and a Cesàro fractal [122] —which in this case is made by drawing a Koch curve [123] with angles of 85°.

The morphologies are clearly different, but are proportioned according to the same ideal ratios. While the ideal tuning for thermal mass governs bulk dimensions, material quantities, temperature attenuation, and buoyancy ventilation, it does not overly determine the choice of form or the spatial layout. Nor does it overly determine the choice of thermal mass material. As the performance data in Fig. 13 show, concrete outperforms hardwood thermally—but surprisingly not by very much. (The hardwood versions have slightly lower values for λ, hence $1 - 1/A_i$ is slightly reduced. The ventilation rate is maintained at $Q = 1\,m^3/s$ by slightly increasing $A*$).

Notice how the wings, courtyard niches, and open plans in Fig. 13 would have very different consequences for the inter-subjective experience of occupants. Working with the ideal massing ratios ($F/\lambda$, Ω) can profoundly but playfully shape the development of an architectural concept from *part to whole*—from the type and thickness of the massing material to the spatial organization of the building.

### 4.4. Limitations

The method is meant to support concept generation and guide engineering studies towards convergence. It is tailored for strategic comparisons at the early stage of design, not absolute forecasts at the later stages of design (c.f. §1). The value for the heat transfer coefficient must be chosen carefully to fairly represent surface heat transfer (c.f. §3.2) and serve as a suitable proxy for average internal loads (c.f. §3.3). A representative range of thermal property values should be used for each candidate material, to reflect the uncertain variation of these properties in the real world (c.f. §4.1). Once a configuration for the building is chosen, Equation (2.16) or Equation (2.17) should be solved to more accurately establish the free-running temperature and ventilation rate. Then further analysis is needed to test the detailed response in a range of scenarios (e.g. anharmonic loads from inside and outside) and to finalize the design (e.g. external insulation, windows, supplementary heating or cooling). One particularly important thing to analyze is how the balance of buoyancy forces, heat loads, and heat storage effects may play out over short and long time scales (§2.1).

## 5. Conclusion

§1 outlined the need for a new approach to building design in the early stages, which allows teams to evaluate the environmental impacts of primary material choices while showing them how to integrate as many functions into these primary materials as possible, so there is less need for other materials, products, and technologies, shrinking the ecological footprint. Shaping one material to integrate structure, thermal mass, and buoyancy ventilation, is a prominent place to start.

§2 showed that, while there has been lots of progress on efficient methods for simulating the effects of thermal mass in arbitrary configurations, none of this new knowledge has been distilled for architects and planners wanting to know how to proportion thermally massive buildings properly, particularly in light of challenges posed by climate change. The work by Holford and Woods [12] was identified as a promising basis for this much-needed design guidance.

§3 found how to optimally synchronize the coupling of internal thermal mass and buoyancy ventilation. The performance of the building is defined by relationship between two parameters: $F/\lambda$ (the ratio of ventilation heat transfer to surface heat transfer) and Ω (the ratio of thermal storage to surface heat transfer). When converted into optimal values, these parameters represent ideal ratios for tuning the form and mass of the building. Design teams can use these ratios to meet chosen targets for the interior temperature and ventilation rate in free-running mode and meaningfully compare the material footprint of design proposals.

§4 demonstrated how to take these ideal ratios ($F/\lambda$, Ω) and materialize them into possible design options. One of the studies suggested that thin-shell structures of minimum weight, and even timber buildings, may be optimally tuned to produce ample ventilation and temperature attenuation (c.f. §4.1). Another study showed how working with these ideal ratios ($F/\lambda$, Ω) could profoundly but playfully shape the development of an architectural concept from part to whole, including the spatial organization of the building, which determines the possible social interactions (c.f. §4.3).

The results of this study imply several avenues for further research. One crucial question is, at what point does the theory break down? For instance, the analysis assumed that a steady, well-mixed, airflow would evolve. For future research, it is necessary to identify other possible flow regimes—steady and transient—and the conditions in which they arise. The influence of climatic conditions, formal/spatial types, and interior load profiles need to be understood, not only for ventilation dynamics, but for thermal comfort and heat stress, too. Comparative life cycle analyses of promising configurations in realistic settings are also needed. Together, this additional research would help extend the method for the later stages of design. As discussed, simulation studies

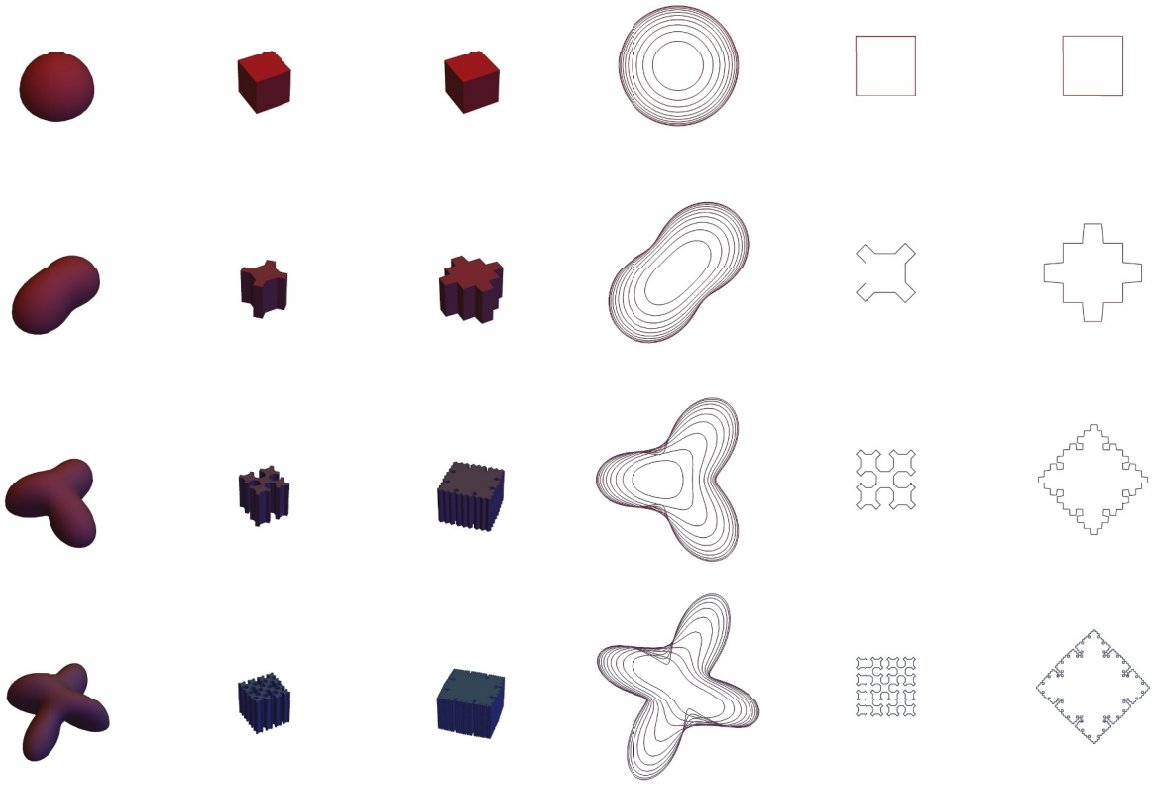

| | Concrete | Hardwood (//) |
|---|---|---|
| S ($m^2$) | 628.3 | 628.3 |
| $\lambda$ | 0.96 | 0.83 |
| $1-1/A_i$ | 0.57 | 0.54 |
| l (cm) | 4.37 | 5.71 |
| V ($m^3$) | 27.4 | 35.9 |
| $A^*(m^2)$ | 1.13 | 1.29 |
| eCO2 (kg) | $(7.1 \pm 1.4) \times 10^3$ | $(-1. \pm 5.) \times 10^4$ |

| | Concrete | Hardwood (//) |
|---|---|---|
| S ($m^2$) | 500 | 500 |
| $\lambda$ | 0.96 | 0.83 |
| $1-1/A_i$ | 0.53 | 0.5 |
| l (cm) | 4.48 | 5.85 |
| V ($m^3$) | 22.4 | 29.3 |
| $A^*(m^2)$ | 1.26 | 1.49 |
| eCO2 (kg) | $(5.8 \pm 1.2) \times 10^3$ | $(-1. \pm 4.) \times 10^4$ |

| | Concrete | Hardwood (//) |
|---|---|---|
| S ($m^2$) | 500. | 500. |
| $\lambda$ | 0.96 | 0.83 |
| $1-1/A_i$ | 0.53 | 0.5 |
| l (cm) | 4.48 | 5.85 |
| V ($m^3$) | 22.4 | 29.3 |
| $A^*(m^2)$ | 1.26 | 1.49 |
| eCO2 (kg) | $(5.8 \pm 1.2) \times 10^3$ | $(-1. \pm 4.) \times 10^4$ |

| | Concrete | Hardwood (//) |
|---|---|---|
| S ($m^2$) | 717.5 | 717.5 |
| $\lambda$ | 0.96 | 0.83 |
| $1-1/A_i$ | 0.59 | 0.57 |
| l (cm) | 4.31 | 5.63 |
| V ($m^3$) | 30.9 | 40.4 |
| $A^*(m^2)$ | 1.07 | 1.2 |
| eCO2 (kg) | $(8.0 \pm 1.6) \times 10^3$ | $(-1. \pm 5.) \times 10^4$ |

| | Concrete | Hardwood (//) |
|---|---|---|
| S ($m^2$) | 825.8 | 825.8 |
| $\lambda$ | 0.96 | 0.83 |
| $1-1/A_i$ | 0.61 | 0.59 |
| l (cm) | 4.25 | 5.56 |
| V ($m^3$) | 35.1 | 45.9 |
| $A^*(m^2)$ | 1.01 | 1.12 |
| eCO2 (kg) | $(9.1 \pm 1.8) \times 10^3$ | $(-2. \pm 6.) \times 10^4$ |

| | Concrete | Hardwood (//) |
|---|---|---|
| S ($m^2$) | 773.1 | 773.1 |
| $\lambda$ | 0.96 | 0.83 |
| $1-1/A_i$ | 0.6 | 0.58 |
| l (cm) | 4.28 | 5.59 |
| V ($m^3$) | 33.1 | 43.2 |
| $A^*(m^2)$ | 1.04 | 1.16 |
| eCO2 (kg) | $(8.6 \pm 1.7) \times 10^3$ | $(-2. \pm 6.) \times 10^4$ |

| | Concrete | Hardwood (//) |
|---|---|---|
| S ($m^2$) | 827.1 | 827.1 |
| $\lambda$ | 0.96 | 0.83 |
| $1-1/A_i$ | 0.61 | 0.59 |
| l (cm) | 4.25 | 5.56 |
| V ($m^3$) | 35.2 | 46. |
| $A^*(m^2)$ | 1.01 | 1.12 |
| eCO2 (kg) | $(9.1 \pm 1.8) \times 10^3$ | $(-2. \pm 6.) \times 10^4$ |

| | Concrete | Hardwood (//) |
|---|---|---|
| S ($m^2$) | 1173. | 1173. |
| $\lambda$ | 0.96 | 0.84 |
| $1-1/A_i$ | 0.67 | 0.65 |
| l (cm) | 4.13 | 5.4 |
| V ($m^3$) | 48.5 | 63.3 |
| $A^*(m^2)$ | 0.916 | 0.985 |
| eCO2 (kg) | $(1.26 \pm 0.25) \times 10^4$ | $(-2. \pm 8.) \times 10^4$ |

| | Concrete | Hardwood (//) |
|---|---|---|
| S ($m^2$) | 1276. | 1276. |
| $\lambda$ | 0.96 | 0.84 |
| $1-1/A_i$ | 0.68 | 0.66 |
| l (cm) | 4.11 | 5.36 |
| V ($m^3$) | 52.4 | 68.4 |
| $A^*(m^2)$ | 0.898 | 0.96 |
| eCO2 (kg) | $(1.36 \pm 0.28) \times 10^4$ | $(-3. \pm 9.) \times 10^4$ |

| | Concrete | Hardwood (//) |
|---|---|---|
| S ($m^2$) | 975.4 | 975.4 |
| $\lambda$ | 0.96 | 0.84 |
| $1-1/A_i$ | 0.64 | 0.62 |
| l (cm) | 4.19 | 5.48 |
| V ($m^3$) | 40.9 | 53.4 |
| $A^*(m^2)$ | 0.961 | 1.05 |
| eCO2 (kg) | $(1.06 \pm 0.21) \times 10^4$ | $(-2. \pm 7.) \times 10^4$ |

| | Concrete | Hardwood (//) |
|---|---|---|
| S ($m^2$) | 1948. | 1948. |
| $\lambda$ | 0.96 | 0.84 |
| $1-1/A_i$ | 0.74 | 0.72 |
| l (cm) | 4.01 | 5.23 |
| V ($m^3$) | 78.1 | 102. |
| $A^*(m^2)$ | 0.831 | 0.869 |
| eCO2 (kg) | $(2.0 \pm 0.4) \times 10^4$ | $(-0.4 \pm 1.4) \times 10^5$ |

| | Concrete | Hardwood (//) |
|---|---|---|
| S ($m^2$) | 2094. | 2094. |
| $\lambda$ | 0.96 | 0.84 |
| $1-1/A_i$ | 0.75 | 0.73 |
| l (cm) | 4. | 5.21 |
| V ($m^3$) | 83.6 | 109. |
| $A^*(m^2)$ | 0.822 | 0.857 |
| eCO2 (kg) | $(2.2 \pm 0.4) \times 10^4$ | $(-0.4 \pm 1.5) \times 10^5$ |

**Fig. 13.** Blobs and castles. These optimized massings have different architectural styles, but all have height H = 10 m and ventilation enough for 100 people (Q = 1 $m^3/s$). As the surface area increases, the floating interior temperature ($1-1/A_i$) cools, and the optimal thickness of thermal mass reduces. Concrete outperforms hardwood thermally, but surprisingly not by very much.

have examined the influence of thermal mass before. However, this study provides a theory for how to dimension the test buildings. It also provides the basis for a new definition of thermal resilience and a functional unit for LCA studies of thermal mass.

## References


[1] H. King, S. Ocko, L. Mahadevan, Termite mounds harness diurnal temperature oscillations for ventilation, Proceedings of the National Academy of Sciences 112 (37) (2015) 11589–11593, https://doi.org/10.1073/pnas.1423242112.

[2] S.A. Ocko, H. King, D. Andreen, P. Bardunias, J.S. Turner, R. Soar, L. Mahadevan, Solar-powered ventilation of African termite mounds, J. Exp. Biol. 220 (18) (2017) 3260–3269, https://doi.org/10.1242/jeb.160895.

[3] S. Craig, Termite Mound Climate Control, (Dec 2017) https://massivesci.com/articles/termite-mound-arcology-climate-control/.

[4] S.A. Ocko, A. Heyde, L. Mahadevan, Morphogenesis of termite mounds, Proceedings of the National Academy of Sciences, vol. 116, 2019, pp. 3379–3384, , https://doi.org/10.1073/pnas.1818759116 9.

[5] M. Vellinga, P. Oliver, A. Bridge, Atlas of Vernacular Architecture of the World, Routledge, 2007.

[6] W. Addis, Building, 3000 Years of Design Engineering and Construction, Phaidon, 2007.

[7] N. Cardinale, G. Rospi, P. Stefanizzi, Energy and microclimatic performance of Mediterranean vernacular buildings: the Sassi district of Matera and the Trulli district of Alberobello, Build. Environ. 59 (2013) 590–598, https://doi.org/10.1016/j.buildenv.2012.10.006.

[8] Passive Solar Buildings, MIT Press, 1992.

[9] J. Clarke, Energy Simulation in Building Design, Routledge, 2007.

[10] C. Underwood, F. Yik, Modelling Methods for Energy in Buildings, John Wiley & Sons, 2008.

[11] J.D. Balcomb, Passive solar research and practice, Energy Build. 7 (4) (1984) 281–295, https://doi.org/10.1016/0378-7788(84)90074-4.

[12] J.M. Holford, A.W. Woods, On the thermal buffering of naturally ventilated buildings through internal thermal mass, J. Fluid Mech. 580 (2007) 3–29, https://doi.org/10.1017/S0022112007005320.

[13] B. Lishman, A.W. Woods, The effect of gradual changes in wind speed or heat load on natural ventilation in a thermally massive building, Build. Environ. 44 (4) (2009) 762–772, https://doi.org/10.1016/j.buildenv.2008.06.026.

[14] G. Reynders, T. Nuytten, D. Saelens, Potential of structural thermal mass for demand-side management in dwellings, Build. Environ. 64 (2013) 187–199, https://doi.org/10.1016/j.buildenv.2013.03.010.

[15] S.I. Seneviratne, M.G. Donat, A.J. Pitman, R. Knutti, R.L. Wilby, Allowable CO2 emissions based on regional and impact-related climate targets, Nature 529 (7587) (2016) 477–483, https://doi.org/10.1038/nature16542.

[16] C.A. Kennedy, I. Stewart, A. Facchini, I. Cersosimo, R. Mele, B. Chen, M. Uda, A. Kansal, A. Chiu, K. gon Kim, C. Dubeux, E.L.L. Rovere, B. Cunha, S. Pincetl, J. Keirstead, S. Barles, S. Pusaka, J. Gunawan, M. Adegbile, M. Nazariha, S. Hoque, P.J. Marcotullio, F.G. Otharán, T. Genena, N. Ibrahim, R. Farooqui, G. Cervantes, A.D. Sahin, Energy and material flows of megacities, Proc. Natl. Acad. Sci. 112 (19) (2015) 5985–5990, https://doi.org/10.1073/pnas.1504315112.

[17] J.M. Allwood, M.F. Ashby, T.G. Gutowski, E. Worrell, Material efficiency: providing material services with less material production, Phil. Trans. R. Soc. Lond. A: Math. Phys. Eng. Sci. 371 (1986) 20120496, https://doi.org/10.1098/rsta.2012.0496 2013.

[18] F. Pomponi, C.D. Wolf, A. Moncaster, Embodied Carbon in Buildings: Measurement, Management, and Mitigation, Springer, 2018.

[19] B. King, The New Carbon Architecture: Building to Cool the Climate, New Society Publishers, 2017.

[20] R. Rovers, Zero-energy and beyond: a paradigm shift in assessment, Buildings 5 (1) (2015) 1–13, https://doi.org/10.3390/buildings5010001.

[21] E. Shove, What is wrong with energy efficiency?, Building Research & Information, 46 (7) (2018) 779–789, https://doi.org/10.1080/09613218.2017.1361746.

[22] F. Pomponi, P.A. Piroozfar, E.R. Farr, An investigation into GHG and non-GHG impacts of double skin façades in office refurbishments, J. Ind. Ecol. 20 (2) (2016) 234–248, https://doi.org/10.1111/jiec.12368.

[23] L. Strain, The Time Value of Carbon: Making the Case for the Importance of Embodied Carbon, Carbon Leadership Forum.

[24] F. Pomponi, A. Moncaster, Embodied carbon mitigation and reduction in the built environment – what does the evidence say? J. Environ. Manag. 181 (2016) 687–700, https://doi.org/10.1016/j.jenvman.2016.08.036.

[25] C.D. Wolf, F. Pomponi, A. Moncaster, Measuring embodied carbon dioxide equivalent of buildings: a review and critique of current industry practice, Energy Build. 140 (2017) 68–80, https://doi.org/10.1016/j.enbuild.2017.01.075.

[26] F. Pomponi, A. Moncaster, C.D. Wolf, Furthering embodied carbon assessment in practice: results of an industry-academia collaborative research project, Energy Build. 167 (2018) 177–186, https://doi.org/10.1016/j.enbuild.2018.02.052.

[27] F. Pomponi, A. Moncaster, Briefing: BS 8001 and the built environment: a review and critique, Proc. Inst. Civ. Eng. - Eng. Sustain. 172 (3) (2018) 111–114, https://doi.org/10.1680/jensu.17.00067.

[28] A.M. Moncaster, F. Pomponi, K.E. Symons, P.M. Guthrie, Why method matters: temporal, spatial and physical variations in LCA and their impact on choice of structural system, Energy Build. 173 (2018) 389–398, https://doi.org/10.1016/j.enbuild.2018.05.039.

[29] A. Dubois, L.-E. Gadde, The construction industry as a loosely coupled system: implications for productivity and innovation, Constr. Manag. Econ. 20 (7) (2002) 621–631, https://doi.org/10.1080/01446190210163543.

[30] M.F. Ashby, J. Fernandez, A. Gray, Unit 9. Architecture & Built Environment: Materials for Construction, Granta CES EduPack 2007, 2007.

[31] B. D'Amico, F. Pomponi, A compactness measure of sustainable building forms, R. Soc. Open Sci. 6 (6) (2019) 181265, https://doi.org/10.1098/rsos.181265.

[32] S.C. Sherwood, M. Huber, An adaptability limit to climate change due to heat stress, Proc. Natl. Acad. Sci. 107 (21) (2010) 9552–9555, https://doi.org/10.1073/pnas.0913352107.

[33] J.S. Pal, E.A.B. Eltahir, Future temperature in southwest Asia projected to exceed a threshold for human adaptability, Nat. Clim. Chang. 6 (2) (2016) 197–200, https://doi.org/10.1038/nclimate2833.

[34] G.P. Henze, J. Pfafferott, S. Herkel, C. Felsmann, Impact of adaptive comfort criteria and heat waves on optimal building thermal mass control, Energy Build. 39 (2) (2007) 221–235, https://doi.org/10.1016/j.enbuild.2006.06.006.

[35] S. Kumar, P. Tewari, S. Mathur, J. Mathur, Development of mathematical correlations for indoor temperature from field observations of the performance of high thermal mass buildings in India, Build. Environ. 122 (2017) 324–342, https://doi.org/10.1016/j.buildenv.2017.06.030.

[36] L.-S. Wang, P. Ma, E. Hu, D. Giza-Sisson, G. Mueller, N. Guo, A study of building envelope and thermal mass requirements for achieving thermal autonomy in an office building, Energy Build. 78 (2014) 79–88, https://doi.org/10.1016/j.enbuild.2014.04.015.

[37] S. Manu, Y. Shukla, R. Rawal, L.E. Thomas, R. de Dear, Field studies of thermal comfort across multiple climate zones for the subcontinent: India Model for Adaptive Comfort (IMAC), Build. Environ. 98 (2016) 55–70 https://doi.org/10.1016/j.buildenv.2015.12.019.

[38] L.A. López-Pérez, J.J. Flores-Prieto, C. Ríos-Rojas, Adaptive thermal comfort model for educational buildings in a hot-humid climate, Build. Environ. 150 (2019) 181–194 https://doi.org/10.1016/j.buildenv.2018.12.011.

[39] M. Vellei, M. Herrera, D. Fosas, S. Natarajan, The influence of relative humidity on adaptive thermal comfort, Build. Environ. 124 (2017) 171–185 https://doi.org/10.1016/j.buildenv.2017.08.005.

[40] E. Barbadilla-Martín, J.M.S. Lissén, J.G. Martín, P. Aparicio-Ruiz, L. Brotas, Field study on adaptive thermal comfort in mixed mode office buildings in southwestern area of Spain, Build. Environ. 123 (2017) 163–175 https://doi.org/10.1016/j.buildenv.2017.06.042.

[41] S. Carlucci, L. Bai, R. de Dear, L. Yang, Review of adaptive thermal comfort models in built environmental regulatory documents, Build. Environ. 137 (2018) 73–89 https://doi.org/10.1016/j.buildenv.2018.03.053.

[42] A. García, F. Olivieri, E. Larrumbide, P. Ávila, Thermal comfort assessment in naturally ventilated offices located in a cold tropical climate, Bogotá, Build. Environ. 158 (2019) 237–247 https://doi.org/10.1016/j.buildenv.2019.05.013.

[43] R. de Dear, J. Kim, T. Parkinson, Residential adaptive comfort in a humid subtropical climate—Sydney Australia, Energy Build. 158 (2018) 1296–1305 https://doi.org/10.1016/j.enbuild.2017.11.028.

[44] Y. Song, Y. Sun, S. Luo, Z. Tian, J. Hou, J. Kim, T. Parkinson, R. de Dear, Residential adaptive comfort in a humid continental climate – tianjin China, Energy Build. 170 (2018) 115–121 https://doi.org/10.1016/j.enbuild.2018.03.083.

[45] D. Sánchez-García, C. Rubio-Bellido, J.J.M. del Río, A. Pérez-Fargallo, Towards the quantification of energy demand and consumption through the adaptive comfort approach in mixed mode office buildings considering climate change, Energy Build. 187 (2019) 173–185 https://doi.org/10.1016/j.enbuild.2019.02.002.

[46] J. Kim, R. de Dear, T. Parkinson, C. Candido, Understanding patterns of adaptive comfort behaviour in the Sydney mixed-mode residential context, Energy Build. 141 (2017) 274–283 https://doi.org/10.1016/j.enbuild.2017.02.061.

[47] E. Barbadilla-Martín, J.G. Martín, J.M.S. Lissén, J.S. Ramos, S. Álvarez Domínguez, Assessment of thermal comfort and energy savings in a field study on adaptive comfort with application for mixed mode offices, Energy Build. 167 (2018) 281–289 https://doi.org/10.1016/j.enbuild.2018.02.033.

[48] A. Pérez-Fargallo, J.A. Pulido-Arcas, C. Rubio-Bellido, M. Trebilcock, B. Piderit, S. Attia, Development of a new adaptive comfort model for low income housing in the central-south of Chile, Energy Build. 178 (2018) 94–106 https://doi.org/10.1016/j.enbuild.2018.08.030.

[49] E.-S. Im, J.S. Pal, E.A.B. Eltahir, Deadly heat waves projected in the densely populated agricultural regions of South Asia, Sci. Adv. 3 (8) (2017) e1603322, https://doi.org/10.1126/sciadv.1603322.

[50] S. Kang, E.A.B. Eltahir, North China Plain threatened by deadly heatwaves due to climate change and irrigation, Nat. Commun. 9 (1) (2018) 2894, https://doi.org/10.1038/s41467-018-05252-y.

[51] Q. Schiermeier, Climate change made Europe's mega-heatwave five times more likely, Nature.

[52] C. Inard, J. Pfafferott, C. Ghiaus, Free-running temperature and potential for free cooling by ventilation: a case study, Energy Build. 43 (10) (2011) 2705–2711 https://doi.org/10.1016/j.enbuild.2011.06.017.

[53] C. Ghiaus, Equivalence between the load curve and the free-running temperature in energy estimating methods, Energy Build. 38 (5) (2006) 429–435 https://doi.org/10.1016/j.enbuild.2005.08.003.

[54] M.J. Holmes, J.N. Hacker, Climate change, thermal comfort and energy: Meeting the design challenges of the 21st century, Energy Build. 39 (7) (2007) 802–814, https://doi.org/10.1016/j.enbuild.2007.02.009.

[55] M.H. Kurth, J.M. Keenan, M. Sasani, I. Linkov, Defining resilience for the US building industry, building research & information 47 (4) (2019) 480–492, https://doi.org/10.1080/09613218.2018.1452489.

[56] A. Baniassadi, J. Heusinger, D.J. Sailor, Energy efficiency vs resiliency to extreme

heat and power outages: the role of evolving building energy codes, Build. Environ. 139 (2018) 86–94 https://doi.org/10.1016/j.buildenv.2018.05.024.
[57] D. Coley, M. Herrera, D. Fosas, C. Liu, M. Vellei, Probabilistic adaptive thermal comfort for resilient design, Build. Environ. 123 (2017) 109–118 https://doi.org/10.1016/j.buildenv.2017.06.050.
[58] K.J. Lomas, R. Giridharan, Thermal comfort standards, measured internal temperatures and thermal resilience to climate change of free-running buildings: a case-study of hospital wards, Build. Environ. 55 (2012) 57–72, https://doi.org/10.1016/j.buildenv.2011.12.006.
[59] L. Yang, Y. Li, Cooling load reduction by using thermal mass and night ventilation, Energy Build. 40 (11) (2008) 2052–2058, https://doi.org/10.1016/j.enbuild.2008.05.014.
[60] E. Krüger, E.G. Cruz, B. Givoni, Effectiveness of indirect evaporative cooling and thermal mass in a hot arid climate, Build. Environ. 45 (6) (2010) 1422–1433, https://doi.org/10.1016/j.buildenv.2009.12.005.
[61] S. Verbeke, A. Audenaert, Thermal inertia in buildings: a review of impacts across climate and building use, Renew. Sustain. Energy Rev. 82 (2018) 2300–2318, https://doi.org/10.1016/j.rser.2017.08.083.
[62] D.G.L. Samuel, S.M.S. Nagendra, M.P. Maiya, Passive alternatives to mechanical air conditioning of building: Areview, Build. Environ. 66 (2013) 54–64, https://doi.org/10.1016/j.buildenv.2013.04.016.
[63] P. Ma, L.S. Wang, Effective heat capacity of interior planar thermal mass (iPTM) subject to periodic heating and cooling, Energy Build. 47 (2012) 44–52, https://doi.org/10.1016/j.enbuild.2011.11.020.
[64] P.F. Linden, G.F. Lane-Serff, D.A. Smeed, Emptying filling boxes: the fluid mechanics of natural ventilation, J. Fluid Mech. 212 (1990) 309–335, https://doi.org/10.1017/S0022112090001987.
[65] P.F. Linden, The fluid mechanics of natural ventilation, Annu. Rev. Fluid Mech. 31 (1) (1999) 201–238, https://doi.org/10.1146/annurev.fluid.31.1.201.
[66] A. Acred, Natural Ventilation in Multi-Storey Buildings: a Preliminary Design Approach, September, 2014.
[67] T. Chenvidyakarn, Buoyancy Effects on Natural Ventilation, Cambridge University Press, Cambridge ; New York, 2013.
[68] A.W. Woods, S. Fitzgerald, S. Livermore, A comparison of winter pre-heating requirements for natural displacement and natural mixing ventilation, Energy Build. 41 (12) (2009) 1306–1312, https://doi.org/10.1016/j.enbuild.2009.07.030.
[69] A.S. Kuesters, A.W. Woods, A comparison of winter heating demand using a distributed and a point source of heating with mixing ventilation, Energy Build. 55 (2012) 332–340, https://doi.org/10.1016/j.enbuild.2012.07.045.
[70] A. Acred, G.R. Hunt, A simplified mathematical approach for modelling stack ventilation in multi-compartment buildings, Build. Environ. 71 (2014) 121–130, https://doi.org/10.1016/j.buildenv.2013.09.004.
[71] A. Acred, G.R. Hunt, Stack ventilation in multi-storey atrium buildings: a dimensionless design approach, Build. Environ. 72 (2014) 44–52, https://doi.org/10.1016/j.buildenv.2013.10.007.
[72] S.A. Gage, G.R. Hunt, P.F. Linden, Top down ventilation and cooling, J. Archit. Plan. Res. 18 (4) (2001) 286–301.
[73] T. Chenvidyakarn, A. Woods, Stratification and oscillations produced by pre-cooling during transient natural ventilation, Build. Environ. 42 (1) (2007) 99–112, https://doi.org/10.1016/j.buildenv.2005.08.007.
[74] T. Chenvidyakarn, A. Woods, Top-down precooled natural ventilation, Build. Serv. Eng. Technol. 26 (3) (2005) 181–193, https://doi.org/10.1191/0143624405bt129oa.
[75] S.R. Livermore, A.W. Woods, On the effect of distributed cooling in natural ventilation, J. Fluid Mech. 600 (2008) 1–17, https://doi.org/10.1017/S0022112007009809.
[76] J. Yam, Y. Li, Z. Zheng, Nonlinear coupling between thermal mass and natural ventilation in buildings, Int. J. Heat Mass Transf. 46 (7) (2003) 1251–1264, https://doi.org/10.1016/S0017-9310(02)00379-4.
[77] J. Zhou, G. Zhang, Y. Lin, Y. Li, Coupling of thermal mass and natural ventilation in buildings, Energy Build. 40 (6) (2008) 979–986, https://doi.org/10.1016/j.enbuild.2007.08.001.
[78] J. Zhou, G. Zhang, Y. Lin, H. Wang, A new virtual sphere method for estimating the role of thermal mass in natural ventilated buildings, Energy Build. 43 (1) (2011) 75–81, https://doi.org/10.1016/j.enbuild.2010.08.015.
[79] T. Chenvidyakarn, A. Woods, Multiple steady states in stack ventilation, Build. Environ. 40 (3) (2005) 399–410, https://doi.org/10.1016/j.buildenv.2004.06.020.
[80] J. Yuan, L.R. Glicksman, Multiple steady states in combined buoyancy and wind driven natural ventilation: the conditions for multiple solutions and the critical point for initial conditions, Build. Environ. 43 (1) (2008) 62–69, https://doi.org/10.1016/j.buildenv.2006.11.035.
[81] N.B. Kaye, Y. Ji, M.J. Cook, Numerical simulation of transient flow development in a naturally ventilated room, Build. Environ. 44 (5) (2009) 889–897, https://doi.org/10.1016/j.buildenv.2008.06.016.
[82] X. Faure, N.L. Roux, Time dependent flows in displacement ventilation considering the volume envelope heat transfers, Build. Environ. 50 (2012) 221–230, https://doi.org/10.1016/j.buildenv.2011.11.007.
[83] D. Yang, Y. Guo, Fluctuation of natural ventilation induced by nonlinear coupling between buoyancy and thermal mass, Int. J. Heat Mass Transf. 96 (2016) 218–230, https://doi.org/10.1016/j.ijheatmasstransfer.2016.01.017.
[84] D. Bastien, A.K. Athienitis, Passive thermal energy storage, part 1: design concepts and metrics, Renew. Energy 115 (2018) 1319–1327, https://doi.org/10.1016/j.renene.2016.04.011.
[85] D. Bastien, A.K. Athienitis, Passive thermal energy storage, part 2: design methodology for solaria and greenhouses, Renew. Energy 103 (2017) 537–560, https://doi.org/10.1016/j.renene.2016.11.041.
[86] C.P. Underwood, An improved lumped parameter method for building thermal modelling, Energy Build. 79 (2014) 191–201, https://doi.org/10.1016/j.enbuild.2014.05.001.
[87] R. Cheng, X. Wang, Y. Zhang, Analytical optimization of the transient thermal performance of building wall by using thermal impedance based on thermal-electric analogy, Energy Build. 80 (2014) 598–612, https://doi.org/10.1016/j.enbuild.2014.05.023.
[88] E. Mantesi, C.J. Hopfe, M.J. Cook, J. Glass, P. Strachan, The modelling gap: quantifying the discrepancy in the representation of thermal mass in building simulation, Build. Environ. 131 (2018) 74–98, https://doi.org/10.1016/j.buildenv.2017.12.017.
[89] W.H. Ko, S. Schiavon, G. Brager, B. Levitt, Ventilation, thermal and luminous autonomy metrics for an integrated design process, Build. Environ. 145 (2018) 153–165, https://doi.org/10.1016/j.buildenv.2018.08.038.
[90] A. Athienitis, W. O'Brien, Modeling, Design, and Optimization of Net-Zero Energy Buildings, John Wiley & Sons, 2015.
[91] J. Hillary, E. Walsh, A. Shah, R. Zhou, P. Walsh, Universal approach to modelling multi-layer structures in building energy simulations, Energy Build. 170 (2018) 122–133, https://doi.org/10.1016/j.enbuild.2018.04.009.
[92] L.-S. Wang, P. Ma, E. Hu, D. Giza-Sisson, G. Mueller, N. Guo, A study of building envelope and thermal mass requirements for achieving thermal autonomy in an office building, Energy Build. 78 (2014) 79–88, https://doi.org/10.1016/j.enbuild.2014.04.015.
[93] J. Hillary, E. Walsh, A. Shah, R. Zhou, P. Walsh, Guidelines for developing efficient thermal conduction and storage models within building energy simulations, Energy 125 (2017) 211–222, https://doi.org/10.1016/j.energy.2017.02.127.
[94] D. Alterman, T. Moffiet, S. Hands, A. Page, C. Luo, B. Moghtaderi, A concept for a potential metric to characterise the dynamic thermal performance of walls, Energy Build. 54 (2012) 52–60, https://doi.org/10.1016/j.enbuild.2012.08.006.
[95] B.M. Jones, M.J. Cook, S.D. Fitzgerald, C.R. Iddon, A review of ventilation opening area terminology, Energy Build. 118 (2016) 249–258, https://doi.org/10.1016/j.enbuild.2016.02.053.
[96] H.B. Awbi, A. Hatton, Mixed convection from heated room surfaces, Energy Build. 32 (2) (2000) 153–166, https://doi.org/10.1016/S0098-8472(99)00063-5.
[97] H.B. Awbi, Calculation of convective heat transfer coefficients of room surfaces for natural convection, Energy Build. 28 (2) (1998) 219–227, https://doi.org/10.1016/S0378-7788(98)00022-X.
[98] A. Novoselac, B.J. Burley, J. Srebric, New convection correlations for cooled ceiling panels in room with mixed and stratified airflow, HVAC R Res. 12 (2) (2006) 279–294, https://doi.org/10.1080/10789669.2006.10391179.
[99] M.A. Menchaca-Brandan, F.A.D. Espinosa, L.R. Glicksman, The influence of radiation heat transfer on the prediction of air flows in rooms under natural ventilation, Energy Build. 138 (2017) 530–538, https://doi.org/10.1016/j.enbuild.2016.12.037.
[100] Handbook of Heat Transfer, McGraw-Hill, 1998.
[101] G. Nellis, S.A. Klein, Heat Transfer, Cambridge University Press, Cambridge; New York, 2009.
[102] M.F. Ashby, Materials and the Environment : Eco-Informed Material Choice, second ed., Elsevier/Butterworth-Heinemann, Amsterdam ; Boston, 2013.
[103] J.N. Hacker, T.P.D. Saulles, A.J. Minson, M.J. Holmes, Embodied and operational carbon dioxide emissions from housing: a case study on the effects of thermal mass and climate change, Energy Build. 40 (3) (2008) 375–384, https://doi.org/10.1016/j.enbuild.2007.03.005.
[104] C.D. Perna, F. Stazi, A.U. Casalena, M. D'Orazio, Influence of the internal inertia of the building envelope on summertime comfort in buildings with high internal heat loads, Energy Build. 43 (1) (2011) 200–206, https://doi.org/10.1016/j.enbuild.2010.09.007.
[105] H. Wang, Q. Chen, A semi-empirical model for studying the impact of thermal mass and cost-return analysis on mixed-mode ventilation in office buildings, Energy Build. 67 (2013) 267–274, https://doi.org/10.1016/j.enbuild.2013.08.025.
[106] T. Wangler, N. Roussel, F.P. Bos, T.A.M. Salet, R.J. Flatt, Digital concrete: a review, Cement Concr. Res. 123 (2019) 105780, https://doi.org/10.1016/j.cemconres.2019.105780.
[107] M. Popescu, L. Reiter, A. Liew, T.V. Mele, R.J. Flatt, P. Block, Building in concrete with an ultra-lightweight knitted stay-in-place formwork: prototype of a concrete shell bridge, Structures 14 (2018) 322–332, https://doi.org/10.1016/j.istruc.2018.03.001.
[108] R.A. Buswell, W.R.L. de Silva, S.Z. Jones, J. Dirrenberger, 3D printing using concrete extrusion: a roadmap for research, Cement Concr. Res. 112 (2018) 37–49, https://doi.org/10.1016/j.cemconres.2018.05.006.
[109] S.J. Keating, J.C. Leland, L. Cai, N. Oxman, Toward site-specific and self-sufficient robotic fabrication on architectural scales, Sci. Robot. 2 (5) (2017) eaam8986, https://doi.org/10.1126/scirobotics.aam8986.
[110] M. West, The Fabric Formwork Book: Methods for Building New Architectural and Structural Forms in Concrete, Routledge, 2016.
[111] S. Adriaenssens, P. Block, D. Veenendaal, C. Williams, Shell Structures for Architecture: Form Finding and Optimization, Routledge, 2014.
[112] D. Veenendaal, M. West, P. Block, History and overview of fabric formwork: using fabrics for concrete casting, Struct. Concr. 12 (3) (2011) 164–177, https://doi.org/10.1002/suco.201100014.
[113] C.D. Oliver, N.T. Nassar, B.R. Lippke, J.B. McCarter, Carbon, fossil fuel, and biodiversity mitigation with wood and forests, J. Sustain. For. 33 (3) (2014) 248–275, https://doi.org/10.1080/10549811.2013.839386.
[114] J.-F. Bastin, Y. Finegold, C. Garcia, D. Mollicone, M. Rezende, D. Routh,

C.M. Zohner, T.W. Crowther, The global tree restoration potential, Science 365 (6448) (2019) 76–79, https://doi.org/10.1126/science.aax0848.
[115] D. Wood, C. Vailati, A. Menges, M. Rüggeberg, Hygroscopically actuated wood elements for weather responsive and self-forming building parts – facilitating upscaling and complex shape changes, Constr. Build. Mater. 165 (2018) 782–791, https://doi.org/10.1016/j.conbuildmat.2017.12.134.
[116] Advancing Wood Architecture, A Computational Approach, first ed., Routledge, London ; New York, 2016.
[117] B. King, The New Carbon Architecture: Building to Cool the Climate, New Society Publishers, 2017.
[118] A. Laborel-Préneron, C. Magniont, J.-E. Aubert, Hygrothermal properties of unfired earth bricks: effect of barley straw, hemp shiv and corn cob addition, Energy Build. 178 (2018) 265–278, https://doi.org/10.1016/j.enbuild.2018.08.021.
[119] D.U. Shah, M.C.D. Bock, H. Mulligan, M.H. Ramage, Thermal conductivity of engineered bamboo composites, J. Mater. Sci. 51 (6) (2016) 2991–3002, https://doi.org/10.1007/s10853-015-9610-z.
[120] E.W. Weisstein, Legendre polynomial, http://mathworld.wolfram.com/LegendrePolynomial.html.
[121] E.W. Weisstein, Sierpiński curve, http://mathworld.wolfram.com/SierpinskiCurve.html.
[122] E.W. Weisstein, Cesàro fractal, http://mathworld.wolfram.com/CesaroFractal.html.
[123] E.W. Weisstein, Koch snowflake, http://mathworld.wolfram.com/KochSnowflake.html.